BUCKLING ANALYSIS OF CARBON NANOTUBE (CNT) REINFORCED LAMINATED COMPOSITE PANELS WITH HOLES

KARBON NANOTÜP (CNT) TAKVİYELİ DELİKLİ LAMİNE KOMPOZİT PANELLERİN BURKULMA ANALİZİ

TOLGAHAN ÖZTÜRK

ASSIST. PROF. DR. MEHMET NURULLAH BALCI

Supervisor

Submitted to

Graduate School of Science and Engineering of Hacettepe University

as a Partial Fulfillment to the Requirements

for the Award of the Degree of Master of Science

in Mechanical Engineering

2024

ABSTRACT

BUCKLING ANALYSIS OF CARBON NANOTUBE (CNT) REINFORCED LAMINATED COMPOSITE PANELS WITH HOLES

Tolgahan ÖZTÜRK

Master of Science, Department of Mechanical Engineering

Supervisor: Assist. Prof. Dr. Mehmet Nurullah BALCI

June 2024, 76 pages

This research offers a thorough examination employing both analytical and computational approaches to ascertain the buckling load of composite plates reinforced with carbon nanotubes (CNTs). The primary goal of this research is to understand and anticipate the buckling effects of composite plates reinforced by carbon nanotubes (CNTs). To achieve this goal, the researchers first analyze the effect of carbon nanotubes (CNTs) on the material's mechanical properties and their influence on elastic properties. Subsequently, the buckling load is analytically computed employing the Classical Laminated Plate Theory (CLPT). Subsequently, numerical methodologies, particularly the finite element method, are utilized to compute the buckling load. The developed computational model is then rigorously validated through comparison with analytical results. Once the model's validation is established, a series of parametric analyses are conducted, encompassing both unperforated and perforated plates. Furthermore, the outcomes of this research are used to provide secondary validation for perforated plates by comparing the findings to those available in the literature. The parametric analyses unveil the diverse effects of variables such as the CNT reinforcement ratio, matrix material properties, stacking lay-up, and hole diameter on the buckling load.

Keywords: Composite laminated structures, Perforated plate, Classical Laminate Plate Theory, Carbon nanotube (CNT), Buckling, Finite element method.

ÖZET

BUCKLING ANALYSIS OF CARBON NANOTUBE (CNT) REINFORCED LAMINATED COMPOSITE PANELS WITH HOLES

Tolgahan ÖZTÜRK

Yüksek Lisans, Makine Mühendisliği

Tez Danışmanı: Dr. Öğr. Üyesi Mehmet Nurullah BALCI

Haziran 2024, 76 sayfa

Bu çalışma, karbon nanotüp (CNT) takviyeli kompozit plakaların burkulma yükünü belirlemek için analitik ve sayısal yöntemlerin birleştirildiği bir araştırmayı sunmaktadır. Araştırmanın temel amacı, CNT takviyeli kompozit plakaların burkulma davranışını anlamak ve bu davranışı tahmin etmektir. Bu amaç doğrultusunda, CNT'lerin malzemenin mekanik özellikleri üzerindeki etkileri incelenmiş ve elastik özelliklerine olan etkileri belirlenmiştir. Ardından, Klasik Laminat Plaka Teorisi (CLPT) kullanılarak analitik bir şekilde burkulma yükü hesaplanmıştır. Daha sonra, sonlu elemanlar yöntemi kullanılarak burkulma yükü sayısal olarak hesaplanmış ve geliştirilen hesaplama modeli, analitik sonuçlarla karşılaştırılarak doğrulanmıştır. Modelin doğrulanmasının ardından, hem deliksiz hem de delikli plakalar için çeşitli parametrik analizler gerçekleştirilmiştir. Ayrıca, literatürde bulunan sonuçlarla bu çalışmada elde edilen sonuçlar karşılaştırılarak delikli plakalar için ikinci bir doğrulama sağlanmıştır. Parametrik analizler, CNT takviye oranı, matris malzemesinin özellikleri, plaka boyutları, delik çapı gibi faktörlerin burkulma yükü üzerindeki etkilerini açıkça ortaya koymuştur.

Anahtar Kelimeler: Kompozit lamine yapılar, Delikli plaka, Klasik Lamine Plaka Teorisi, Karbon nanotüp(CNT), Burkulma, Sonlu elemanlar yöntemi.

ACKNOWLEDGMENTS

I am deeply grateful to my thesis adviser, Assist. Prof. Dr. Mehmet Nurullah BALCI, for his great advice, constant support, and patience during the completion of this work. His guidance and support were important in defining my study and guiding me through its complexity. I'm grateful to him for his effort and essential assistance.

I am grateful to my spouse, Çiğdem ÖZTÜRK, for her continuous support, comprehension, and inspiration during this attempt. Her unwavering faith in me has acted as an endless source of reassurance. Her love and support have enabled me to fully pursue my academic goals, and I am very thankful for her commitment to our shared path.

To my mother, Hatice ÖZTÜRK, my father, İsmail ÖZTÜRK, and my brother, Buğrahan Mutlu ÖZTÜRK, I am indebted for their endless love, support, and faith in my capabilities. They gave me as much as they could throughout my entire education and life. Their unwavering support has been a source of strength all along this path.

I also want to extend my gratitude to Mustafa KUTLU, my head engineer at work, for his understanding, flexibility, and support during times when I needed to focus on my thesis. His guidance has been instrumental in balancing my professional responsibilities with my academic pursuits.

Lastly, my gratitude goes out to all those who have supported me in various ways, whether through their encouragement, advice, or assistance. Your feedback and suggestions were crucial in completing this study.

I want to thank everyone for their support and assistance during this trip.

TABLE OF CONTENTS

LIST OF FIGURES

LIST OF TABLES

SYMBOLS AND ABBREVIATIONS

Symbols

u, v, w	:	Displacement components along the x, y, and z axes, respectively
u_o, v_o	:	In-plane displacement at a point of the mid-plane
$\varepsilon_x, \varepsilon_y$	:	Normal strains within the plane
γ_{xy}	:	Shear strain within the plane
$\varepsilon_x^O, \varepsilon_y^O, \gamma_{xy}^O$	:	Strains at the mid-plane
K_x, K_y, K_{xy}	:	Changes in curvature of the mid-plane during deformation
N_x, N_y, N_{xy}	:	Resultant stresses within the plane
M_x, M_y, M_{xy}	:	Resultant moments within the plane
σ_x, σ_y	:	Normal stresses within the plane
τ_{xy}	:	Shear stress within the plane
z_k	:	Distance from the top point of a ply to the mid-plane.
k	:	Layer number
N	:	Number of layers
h	:	Thickness of plate
Q_{ij}	:	The reduced stiffness
E	:	Modulus of Elasticity
G	:	Shear Modulus
υ	:	Poisson's Ratio
$\overline{Q_{ij}}$	:	The transformed reduced stiffness matrix elements
θ	:	Fiber orientation
A_{ij}, B_{ij}, D_{ij}	:	Stiffness coefficients
$\Delta_{D_{ij}}$	:	Percentage difference from when volume fraction is 0%
t_k	:	Thickness of layer
P_x , P_y , q	:	Pressure components
Q_x, Q_y	:	Forces representing transverse shear
L_{ij}	:	Differential operators that symbolize the stiffness characteristics of the plate
F	:	Differential operator that symbolize the loading applied within the plane
a	:	Length of plate

b	:	Width of plate
a/b	:	Ratio of the length of the long edge to that of the short edge
C_{mn}	:	Coefficient of small arbitrary amplitude
m	:	The number of half-waves in the x directions
n	:	The number of half-waves in the y directions
$(N_{xx})_{cr}$	:	Critical buckling load
λ	:	Parameter chosen appropriately to meet boundary conditions
V_i	:	Volume fraction
L_{cnt}	:	Length of the nanotube
d_{cnt}	:	Outer diameter of the nanotube
f_R	:	Orientation factor of CNTs
f_W	:	Waviness factor
f_A	:	Agglomeration efficiency factor
A	:	Amplitude of CNT
W	:	Half wavelength of CNT
ρ_i	:	Density
η	:	Experimental factor
ξ	:	Reinforcing factor
c	:	Minor radius of hole
d	:	Major radius of hole
β	:	Angle of hole with the x-axis

Abbreviations

CNT	:	Carbon Nanotube
SWCNT	:	Single wall carbon nanotube
MWCNT	:	Multi-wall carbon nanotube
CVD	:	Chemical vapor deposition
CLPT	:	Classical laminated plate theory
FEM	:	Finite element method
CNTR-FG	:	Carbon nanotube reinforced functionally graded
FSDT	:	First-order shear deformation theory
SSSS	:	Plate supported on all sides with simple supports.
CCSS	:	Plate clamped on the short edge and simply supported on the long edge.
SSCC	:	Plate simply supported on the short edge and clamped on the long edge.
CCCC	:	Clamped on all sides of plate
SSSF	:	Plate simply supported on three edges and free on one edge.
H-T	:	Halpin-Tsai

1. INTRODUCTION

The aerospace industry is relying more on advanced materials like composites for better structural performance, i.e., low weight and high strength/stiffness. These requirements can be met with composite materials. Composites are frequently used in airplanes, cars, and the aerospace industry because they provide low weight, high fatigue strength and low corrosion. To give an example, Figure 1.1 depicts the materials utilized in the construction of the Boeing 787.

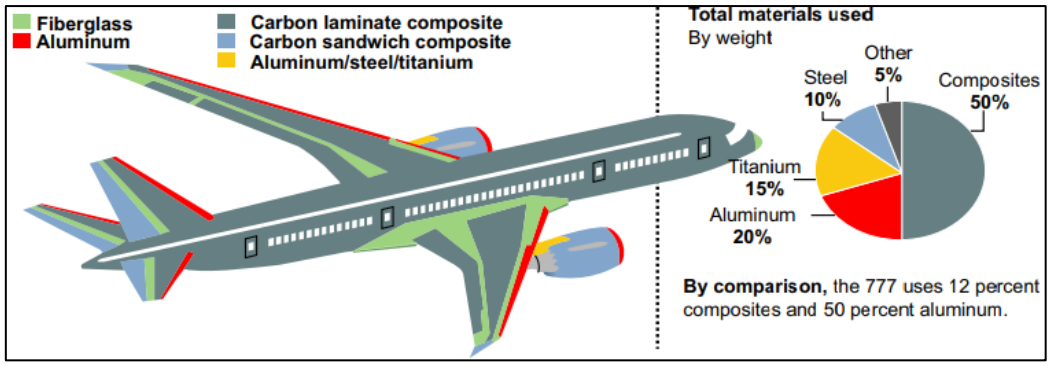

Figure 1.1. The materials employed in the manufacturing of the Boeing 787 [1].

It is possible to increase certain strength aspects of composites without compromising the structure by introducing carbon nanotubes (CNT) into resin. Carbon nanotubes (CNTs) have sparked widespread industrial interest due to their superior mechanical, electrical, thermal, chemical, and even biological properties. The image showing the structure of the carbon nanotube is given in Figure 1.2.

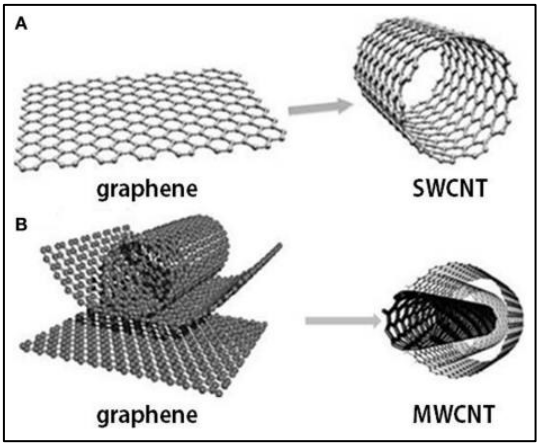

Figure 1.2. Graphene and carbon nanotubes as (A) single wall carbon nanotube (SWCNT) and (B) multi-wall carbon nanotube (MWCNT) structures [2].

1.1. Purpose of Thesis

The aim of this research is to investigate how a specific amount of carbon nanotubes (CNTs) added to a composite material affects its buckling behavior. To evaluate the influence of CNT reinforcement on the buckling of perforated composite panels, a finite element analysis was carried out. The panels under consideration are rectangular and have symmetric lamination, with all edges being simply supported as the boundary condition.

1.2. Literature Review

Scientist Sumio Iijima [3] from Japan made the initial discovery of carbon nanotubes in 1991. Iijima, who works for NEC Company, found a thin rod in filaments made between graphite electrodes using electron microscopy. He later identified the rods as "carbon nanotubes" after observing that the carbon atoms were grouped in an orderly pattern.

Due to its characteristics, including electrical conductivity, mechanical strength, heat resistance, large surface area, and chemical resistance, carbon nanotubes are employed in a variety of industries. Examples include:

- Electronics: By substituting semiconductor materials, carbon nanotubes might make it possible to build electronic devices that are quicker, smaller, more powerful, and more efficient.
- Materials science: Polymers, metals, and ceramics can be filled with carbon nanotubes to enhance their mechanical, electrical, and thermal characteristics.
- Biotechnology: Carbon nanotubes are useful in biotechnology because they may be employed as drug carriers, biosensors, and other biological devices.
- Space technology: Carbon nanotubes can be utilized in space technology to create materials that are strong, lightweight, and thermally insulated for spacecraft.
- Sporting material: Carbon nanotubes can be utilized to create strong and lightweight materials for sporting goods.

The production of carbon nanotubes can be accomplished by various methods [4]. These methods can be listed as follows.

- Chemical Vapor Deposition (CVD) Method: In this technique, high temperatures are applied to carbon sources like methane, ethylene, or benzene. Carbon atoms agglomerate and develop into nanotubes on a metal catalyst when hot gases are cooled there. This technique is widely used to create carbon nanotubes with high purity.
- Electric Arc Discharge Method: In this process, the space between graphite electrodes is filled with an electric current. The graphite electrodes are melted during this procedure, and the molten carbon atoms unite to form nanotubes. This approach often results in shorter nanotubes with a heterogeneous structural makeup.
- Laser Ablation Method: This method involves focusing a laser beam on a graphite substrate, causing it to vaporize. The carbon atoms that evaporate subsequently cool down to the surrounding temperature and condense to form nanotubes.

These methods each have advantages and disadvantages and create nanotubes with different properties.

Soni et al. [6] investigated the details of the characteristics and uses of CNT-reinforced nanocomposites. The research described various methods of creating nanotubes, such as arc discharge, laser ablation, and chemical vapor deposition. It also outlined the techniques used for dispersing, functionalizing, and purifying carbon nanotubes, with reference to previously published studies.

Dindar [5], in his work, produced a composite plate containing carbon nanotubes. The figures presented below offer an instance of how the production of nanotubes can be carried out.

Figure 1.3. Epoxy resin and CNT with 0.5% [5]

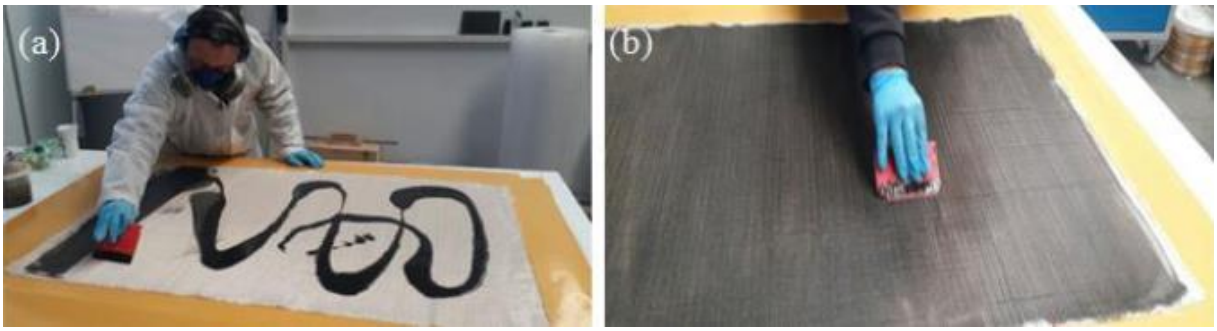

Figure 1.4. Hand lay-up method (a), application of resin-particle solution to glass fiber (b) [5]

Buckling is a type of structural instability that can cause material structural damage. It is also known as elastic instability. Buckling can cause structures to rupture or separate. Buckling can also occur in the absence of a rupture or separation. Buckling behavior is influenced by the aspect ratio and thickness of the material.

Researchers have conducted substantial work to comprehend the performance of metal buckling in general. There have been many different studies on flat plate buckling in the literature. Leissa [1] derived plate buckling equations and analyzed plate bifurcation buckling. In addition, Timoshenko and Gere [8] added differential equations to the literature under different load conditions and boundary conditions. In a finite element analysis program like ANSYS, studies were undertaken by Hassan and Kurgan [9] to validate the theories and solutions for plate buckling that were put forth. In this study, the convergence of the plate meshes was examined utilizing shell and various solid elements. Research was conducted to analyze the impact of aspect ratio and side-to-thickness ratio on the critical buckling load. The study was carried out under different boundary conditions to obtain conclusive results. Pouladkhan [10] investigated how thin plates buckle under various boundary conditions. The critical load was examined using the equilibrium method, which is the most popular method. The methodology is based on resolving a partial differential equation of fourth order. To investigate the finite element model, the software ABAQUS was utilized in the research. Several automotive, aerospace, and associated industries require perforated plates for maintenance, access, and inspection. It is necessary to use software for finite element analysis because it is difficult to mathematically determine the buckling load of perforated plates. Nevertheless, Chow and Narayanan [11] conducted research on the way a perforated plate behaves when it is subjected to different loads and placed under various boundary conditions, paying particular attention to its buckling behavior. According to the diameter and eccentricity of the hole, they evaluated at several parameters, and the appropriate finite element formulation was presented and debated. Experiments have been done to validate this formulation in studies. In terms of hole shapes,

slenderness ratios, and hole diameter parameters, Uslu et al.'s [12] investigation focused on the critical buckling loads of thin plates with round and square perforations, uniaxially loaded, and simply supported with boundary conditions. The structural shell element used for examining the models was Shell-181, which comprised 4 nodes. This element was sourced from ANSYS, a finite element program library. When comparing the critical buckling load of plates with square and circular holes, it was discovered that plates with square holes can sustain greater forces before buckling than plates with circular perforations.

Plate theory was adopted and modified for analysis of laminate composite plates. Stephen Tsai [13] and some researchers explained Classical Laminate Theory. Kaw [15] explained the basic definitions of composite mechanics, explained the difference between lamina and laminate, and discussed their mechanical behavior. Whitney [16] made a thorough examination of the structural behavior of laminated plates. The work established a solid basis in laminated anisotropic plate theory, including analyses of bending under transverse stress, stability, and free-vibration issues. Kassapoglou [17] developed different solution methods using classical laminated-plate (CLPT), energy methods, and Rayleigh-Ritz approaches, and Chapter 6 includes discussions about the buckling of the composite plate. He explained the critical buckling equations according to different wave numbers, and different load and boundary conditions. Nemeth [18] deduced dimensionless material coefficients from the governing buckling equation and proposed a dimensionless parameter for determining whether anisotropic bending stiffnesses can be ignored. Through finite element analysis, he discovered how anisotropic bending stiffnesses are influenced by factors such as fiber alignment, aspect ratio, constraints, lay-up sequence, and thickness. Doğan [19] examined the buckling analysis of symmetric composite laminates that were thin and thick under a simple support boundary condition. Using the Hamilton's principle, he was able to develop an equation that describes the motion of a laminated rectangular plate that is both thin and thick and is subject to in-plane loads. The solutions are compiled using the Navier approach technique. In this study, the buckling analysis of a rectangular plate was investigated in terms of anisotropy and edge ratios. The ANSYS software was used to compare the values obtained from the theoretical and numerical solutions. Yıldırım et al. [20] examined buckling analysis in orthotropic plates. Xiang et al. [21] used higher-order deformation theory due to shear to compute the critical buckling load of a composite plate that was simply supported. They used the Navier analytical solution to solve the resultant equation and calculated the critical buckling loads using a variety of geometrical and material factors. The outcomes were contrasted with the results of previous

research that had been published. In research done by Nemeth [22], the buckling of a rectangular plate with a center circular hole was explored utilizing finite element computations, testing, and approximation analysis. The plate was compared to a symmetric laminated angled ply plate, and the study revealed the effects of variables such as hole size, aspect proportion, loading, and boundaries. Han et al. [23] studied the buckling influence of fibers positioned at different angles on a composite laminate that had and did not have holes when compressed. They demonstrated that the variable-angle laminates considerably enhanced the buckling load while dramatically reducing the maximum in-plane stress. It was discovered that the presence of holes had a deleterious influence on the critical buckling load. Moreover, the stiffness of the fibers positioned at different angles also lessens.

Since studies on Carbon Nanotube have just been developed, there are not many such examinations in the literature. Georgantzinos et al. [24] used the finite element approach to investigate the buckling of layered composite rectangular plates strengthened with multi-walled carbon nanotubes (MWCNT). The modulus of elasticity of the composite matrix was determined using the rule of mixtures and the Halpin-Tsai method. The study looked at the influence of three essential aspects on material properties: arbitrary distribution, waviness, and aggregation of MWCNT. Reddy et al. [25] used ANSYS software and numerical simulation to investigate the free vibration of composite laminate panels enhanced with carbon nanotubes. Reddy used numerical homogenization to compute the elastic characteristics of composites reinforced with arbitrarily dispersed carbon nanotubes. Taş and Soykok [26] calculated the engineering factors for a composite laminate enhanced with carbon nanotubes. Three-point bending analysis was conducted individually under concentrated and distributed load. Lei et al. [27] investigated the buckling behavior of laminated plates composed of a carbon-nanotube reinforced functionally graded (CNTR-FG) composite. The first-order shear deformation theory (FSDT) was used to account for transverse shear deformation and rotational inertia. The buckling solution was obtained using the meshless kp-Ritz technique. The study investigated the effect of different ply angles, rigidity ratios, boundary and loading conditions, carbon nanotube volume fractions, and plate length divided by thickness ratios on buckling loading.

In literature, there are not many papers containing composite plate buckling analyses with holes in different cut-outs. Finding the critical load that causes the buckling of a plate with various shaped holes using numerical methods is difficult owing to its complexity. This is because the presence of holes in a composite plate can cause complicated stress distributions in the plate, which can result in unexpected buckling behavior. Analyzing this behavior is a difficult task,

and as such, there have not been many papers dedicated to this topic. For this reason, we use the finite element approach and accompanying software like Simcenter. The general purpose of the study is to examine the critical buckling load of a CNT-reinforced composite plate with different shapes of holes. Ouinas and Achour [28] conducted a significant study that delved into the buckling load of a composite plate with varying shapes. An investigation was conducted on the critical buckling load of an elliptical notch composite plate. The study considered several factors, such as the plate's fiber orientation, notch position, notch length ratio, rigidity ratio, and thickness. The outcomes demonstrate that the buckling load, which is essential to the composite plate, went down as the notch length ratio and position rose. Furthermore, the critical buckling load was shown to go upward with plate thickness and lessen with the rigidity ratio. The study by Kumar et al. [29] can be shown as another example of studies with different shaped holes. Kumar et al. investigated the buckling reaction of plates made of composites under in-plane loads. The study focused on plates with varied cut-outs, such as squares and rectangles. They used clamped-free-clamped-free as the boundary condition for the plate in their investigation, and as a consequence, both numerical and experimental results were attained. Prior to performing the study of the composite plate, they first performed a buckling analysis of the aluminum plate to validate the analytical methodology. The study looked at how critical buckling stress influences aspect ratio, length divided by thickness ratio, ply alignment, and multiple cut-outs. Circular cut-out has more critical buckling loads than square and rectangular cut-outs. In addition, rectangular forms provide a particularly low critical buckling load.

2. Modelling of Plate Buckling

2.1. Introduction

Thin plates have become a key component in many technical applications in contemporary times. Under certain load circumstances, such as compression and shear, these plates may buckle. The formulae for estimating the critical buckling loads of governing plates are included. These equations assist in determining the point at which the plates will buckle. The formulas used in this section to derive the plate buckling equations are provided by A. W. Leissa [1]. For the sake of brevity, not all details are provided.

2.2. Plate Stiffness Equations

The Kirchhoff hypothesis gave rise to the classical plate theory. The z-axis is also in the out-of-plane direction if x-axis and y-axis are considered plate directions. Plate's central will not be warped and will remain flat, but the plate's surface will be deformed. The Figure 2.1, contributed by Robert M. Jones [30], better demonstrates this definition.

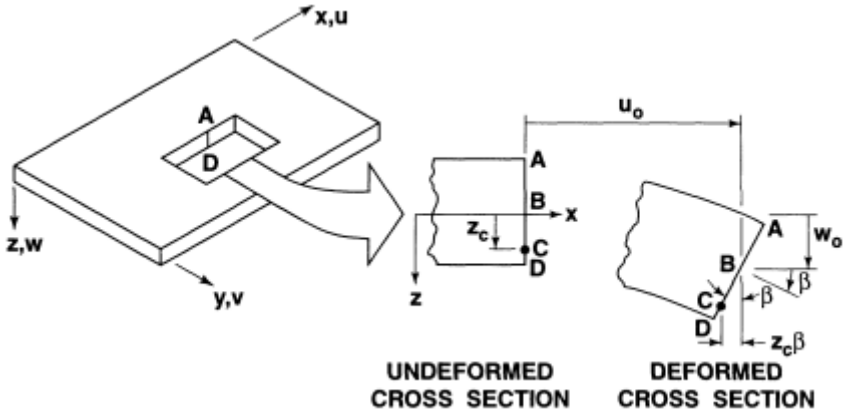

Figure 2.1. Deformation Geometry within the x-z Plane [30].

Based on this visualization, the kinematic behavior of the plate is defined in the equations below.

$$u = u_o - z\frac{\partial w}{\partial x}$$

$$v = v_o - z\frac{\partial w}{\partial y} \tag{2.1}$$

u, v, and w can be used to represent any point on the plate, whereas u_o and v_o can represent in-plane displacements at any position on a plate's mid-surface. The equations below are the strain-displacement equations of classical planar elasticity theory.

$$\varepsilon_x = \frac{\partial u}{\partial x}, \qquad \varepsilon_y = \frac{\partial v}{\partial y}, \qquad \gamma_{xy} = \frac{\partial v}{\partial x} + \frac{\partial u}{\partial y} \tag{2.2}$$

Rearranging and rewriting Eq. (2.1) yields the following equations, with ε_x and ε_y representing in-plane normal strains and γ_{xy} denoting in-plane engineering shear strain.

$$\begin{aligned} \varepsilon_x &= \varepsilon_x^O - zK_x \\ \varepsilon_y &= \varepsilon_y^O - zK_y \\ \gamma_{xy} &= \gamma_{xy}^O - zK_{xy} \end{aligned} \tag{2.3}$$

The middle-surface strains are denoted by ε_x^O, ε_y^O and γ_{xy}^O, whereas the changes in curvature throughout deformation are represented by K_x, K_y, and K_{xy}. These quantities are exclusively reliant on x and y and are stated as functions of them.

$$\varepsilon_x^O = \frac{\partial u_O}{\partial x}, \qquad \varepsilon_y^O = \frac{\partial v_O}{\partial y}, \qquad \gamma_{xy}^O = \frac{\partial v_O}{\partial x} + \frac{\partial u_O}{\partial y} \tag{2.4}$$

$$K_x = \frac{\partial^2 w}{\partial x^2}, \qquad K_y = \frac{\partial^2 w}{\partial y^2} \qquad K_{xy} = 2\frac{\partial^2 w}{\partial x \partial y} \tag{2.5}$$

The procedure entails computing the combined strains over the thickness of a material. This calculation yields the resulting forces and moments per unit length.

$$\begin{bmatrix} N_x \\ N_y \\ N_{xy} \end{bmatrix} = \int_{-\frac{h}{2}}^{\frac{h}{2}} \begin{bmatrix} \sigma_x \\ \sigma_y \\ \tau_{xy} \end{bmatrix} dz \tag{2.6}$$

$$\begin{bmatrix} M_x \\ M_y \\ M_{xy} \end{bmatrix} = \int_{-\frac{h}{2}}^{\frac{h}{2}} \begin{bmatrix} \sigma_x \\ \sigma_y \\ \tau_{xy} \end{bmatrix} z dz \tag{2.7}$$

Figure 2.2 depicts the forces operating in the plane, including normal forces N_x and N_y (as per length), in-plane shear forces N_{xy}, and transverse shear forces Q_x and Q_y. Figure 2.3 also displays the moments of bend M_x and M_y, as well as the twisting moment M_{xy}.

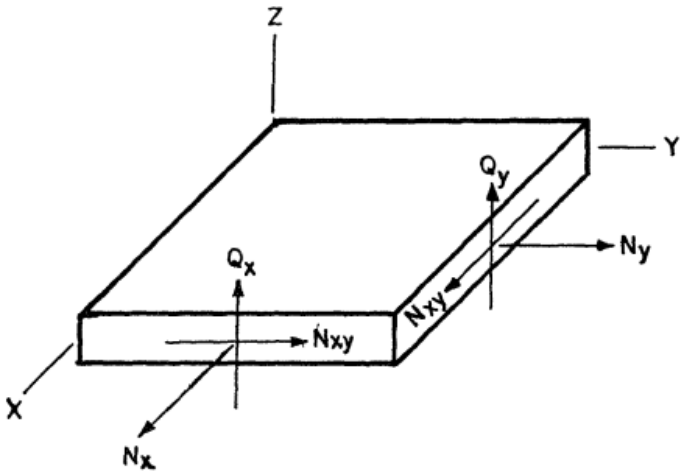

Figure 2.2. Stress Resultants [1].

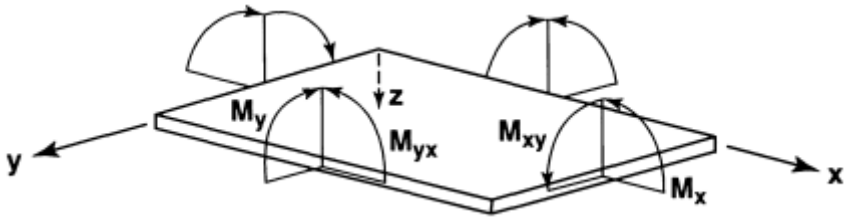

Figure 2.3. Moment Resultants [30].

However, because we have seen that stress distribution is discontinuous across plies in the real laminate when the plies change orientations, we have difficulty integrating stress over thickness across the whole laminate thickness. As a result, we must do the stress integral over the thickness of the laminae rather than the thickness of the laminate. We must then repeat the integral for each lamina thickness and combine them together.

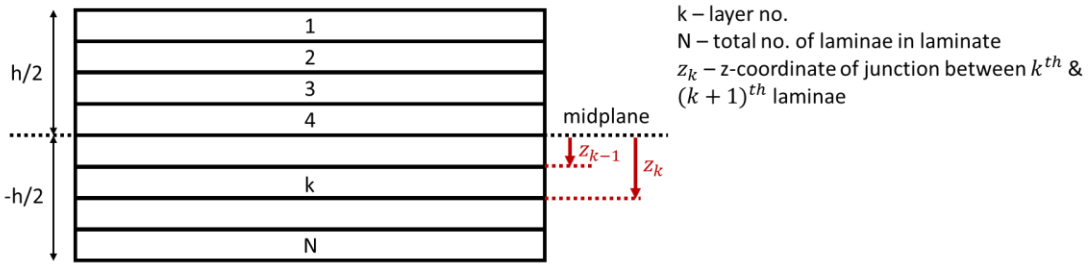

Figure 2.4. Lay-out of a N-Layered Laminated Plate.

$$\begin{bmatrix} N_x \\ N_y \\ N_{xy} \end{bmatrix} = \int_{-\frac{h}{2}}^{\frac{h}{2}} \begin{bmatrix} \sigma_x \\ \sigma_y \\ \tau_{xy} \end{bmatrix} dz = \sum_{k=1}^{N} \int_{z_{k-1}}^{z_k} \begin{bmatrix} \sigma_x \\ \sigma_y \\ \tau_{xy} \end{bmatrix}_k dz \tag{2.8}$$

$$\begin{bmatrix} M_x \\ M_y \\ M_{xy} \end{bmatrix} = \int_{-\frac{h}{2}}^{\frac{h}{2}} \begin{bmatrix} \sigma_x \\ \sigma_y \\ \tau_{xy} \end{bmatrix} z dz = \sum_{k=1}^{N} \int_{z_{k-1}}^{z_k} \begin{bmatrix} \sigma_x \\ \sigma_y \\ \tau_{xy} \end{bmatrix}_k z dz \tag{2.9}$$

Before proceeding with the calculations, some terms need to be defined. The equation below depicts the stress-strain relationship for an orthotropic plate exposed to planar stress.

$$\begin{bmatrix} \sigma_1 \\ \sigma_2 \\ \tau_{12} \end{bmatrix} = \begin{bmatrix} Q_{11} & Q_{12} & 0 \\ Q_{12} & Q_{22} & 0 \\ 0 & 0 & Q_{66} \end{bmatrix} \begin{bmatrix} \varepsilon_1 \\ \varepsilon_2 \\ \gamma_{12} \end{bmatrix} \tag{2.10}$$

Where Q_{ij} are the reduced stiffnesses. For the orthotropic lamina, the Q_{ij} is given below.

$$Q_{11} = \frac{E_1}{1 - \upsilon_{12}\upsilon_{21}}$$

$$Q_{22} = \frac{E_2}{1 - \upsilon_{12}\upsilon_{21}} \tag{2.11}$$

$$Q_{12} = \frac{\upsilon_{12}E_2}{1 - \upsilon_{12}\upsilon_{21}} = \frac{\upsilon_{21}E_1}{1 - \upsilon_{12}\upsilon_{21}}$$

$$Q_{66} = G_{12}$$

Poisson's Ratio, the connection between two forms of deformation, may be described in terms of elastic and shear moduli E_1, E_2, and G_{12}. The connection between υ_{12} and υ_{21} may be determined from these moduli.

$$\frac{\upsilon_{12}}{E_1} = \frac{\upsilon_{21}}{E_2} \tag{2.12}$$

The stress and strain properties of an orthotropic material have been studied using primary material coordinates. Figure 2.5 depicts potential changes in laminate orientation.

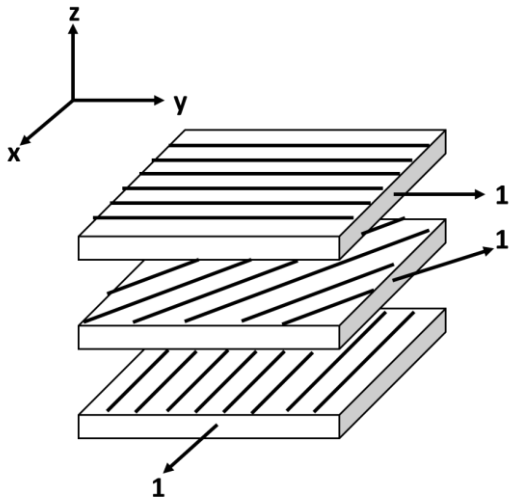

Figure 2.5. 3-Layered Panel.

A correlation between the stresses and strains in the material's main coordinates and the body coordinates needs to exist. The lamina's stress-strain connections in the x-y plane are shown below.

$$\begin{bmatrix} \sigma_1 \\ \sigma_2 \\ \tau_{12} \end{bmatrix} = \begin{bmatrix} \overline{Q_{11}} & \overline{Q_{12}} & \overline{Q_{16}} \\ \overline{Q_{12}} & \overline{Q_{22}} & \overline{Q_{26}} \\ \overline{Q_{16}} & \overline{Q_{16}} & \overline{Q_{66}} \end{bmatrix} \begin{bmatrix} \varepsilon_1 \\ \varepsilon_2 \\ \gamma_{12} \end{bmatrix} \tag{2.13}$$

The following equations show the elements of $\overline{Q_{ij}}$ in terms of the reduced stiffnesses Q_{ij}. The transformed reduced stiffnesses are denoted by $\overline{Q_{ij}}$.

$$\begin{aligned} \overline{Q_{11}} &= Q_{11}\cos^4\theta + 2(Q_{12} + 2Q_{66})\sin^2\theta\cos^2\theta + Q_{22}\sin^4\theta \\ \overline{Q_{12}} &= (Q_{11} + Q_{12} - 4Q_{66})\sin^2\theta\cos^2\theta + Q_{12}(\sin^4\theta\, cos^4\theta) \\ \overline{Q_{22}} &= Q_{11}\, sin^4\theta + 2(Q_{12} + 2Q_{66})\sin^2\theta\cos^2\theta + Q_{22}\, cos^4\theta \end{aligned} \tag{2.14}$$

$$\overline{Q_{66}} = (Q_{11} + Q_{22} - 2Q_{12} - 2Q_{66})\sin^2\theta\cos^2\theta + Q_{66}(\sin^4\theta\, cos^4\theta)$$

In Figure 2.6, the angle between the x-axis and the 1-axis is denoted by θ.

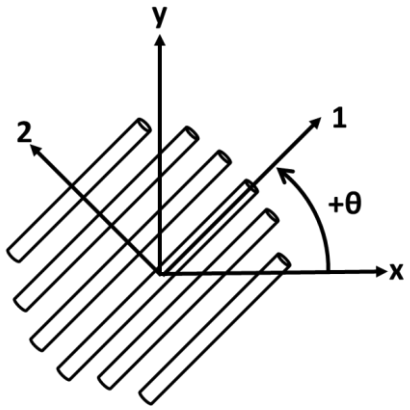

Figure 2.6. Change in Orientation of Primary Material Coordinates from the x and y Axes.

After finding the $\overline{Q_{\iota J}}$, we have already established an expression for layer stresses in terms of transformed stiffness and mid-surface curvatures (Eq. 2.3). Substituting this equation into Eq. (2.8) and Eq. (2.9) and moving out $[\bar{Q}]_k$ outside the integral as it does not vary through z is obtained.

$$\begin{bmatrix} N_x \\ N_y \\ N_{xy} \end{bmatrix} = \sum_{k=1}^{N} [\bar{Q}]_k \left\{ \int_{z_{k-1}}^{z_k} \begin{bmatrix} \varepsilon_x^O \\ \varepsilon_y^O \\ \gamma_{xy}^O \end{bmatrix} dz + \int_{z_{k-1}}^{z_k} \begin{bmatrix} K_x \\ K_y \\ K_{xy} \end{bmatrix} z dz \right\} \tag{2.15}$$

$$\begin{bmatrix} N_x \\ N_y \\ N_{xy} \end{bmatrix} = \sum_{k=1}^{N} \left\{ [\bar{Q}]_k (z_k - z_{k-1}) \{\varepsilon^O\}_k + [\bar{Q}]_k \left(\frac{z_k^2}{2} - \frac{z_{k-1}^2}{2} \right) \{K^O\}_k \right\} \tag{2.16}$$

$$\{N\} = [A]\{\varepsilon^O\}_k + [B]\{K^O\}_k \tag{2.17}$$

And,

$$\begin{bmatrix} M_x \\ M_y \\ M_{xy} \end{bmatrix} = \sum_{k=1}^{N} [\bar{Q}]_k \left\{ \int_{z_{k-1}}^{z_k} \begin{bmatrix} \varepsilon_x^O \\ \varepsilon_y^O \\ \gamma_{xy}^O \end{bmatrix} z dz + \int_{z_{k-1}}^{z_k} \begin{bmatrix} K_x \\ K_y \\ K_{xy} \end{bmatrix} z^2 dz \right\} \tag{2.18}$$

$$\begin{bmatrix} M_x \\ M_y \\ M_{xy} \end{bmatrix} = \sum_{k=1}^{N} \left\{ [\bar{Q}]_k \left(\frac{z_k^2}{2} - \frac{z_{k-1}^2}{2} \right) \{\varepsilon^O\}_k + [\bar{Q}]_k \left(\frac{z_k^3}{2} - \frac{z_{k-1}^3}{2} \right) \{K^O\}_k \right\} \tag{2.19}$$

$$\{M\} = [A]\{\varepsilon^O\}_k + [D]\{K^O\}_k \tag{2.20}$$

After doing the appropriate computations, the stress and moment results may be connected to mid-plane strains and curvature changes, as shown in the equation below.

$$\begin{bmatrix} N_x \\ N_y \\ N_{xy} \\ - \; - \\ M_x \\ M_y \\ M_{xy} \end{bmatrix} = \left[\begin{array}{ccc|ccc} A_{11} & A_{12} & A_{16} & B_{11} & B_{12} & B_{16} \\ A_{12} & A_{22} & A_{26} & B_{12} & B_{22} & B_{26} \\ A_{16} & A_{26} & A_{66} & B_{16} & B_{26} & B_{66} \\ - \; - & - \; - & - \; - & - \; - & - \; - & - \; - \\ B_{11} & B_{12} & B_{16} & D_{11} & D_{12} & D_{16} \\ B_{12} & B_{22} & B_{26} & D_{12} & D_{22} & D_{26} \\ B_{16} & B_{26} & B_{66} & D_{16} & D_{26} & D_{66} \end{array}\right] \begin{bmatrix} \varepsilon_x^O \\ \varepsilon_y^O \\ \gamma_{xy}^O \\ - \\ -K_x \\ -K_y \\ -K_{xy} \end{bmatrix} \tag{2.21}$$

Where the A_{ij} are extensional stiffnesses, the B_{ij} are bending-extension coupling stiffnesses, and the D_{ij} are bending stiffnesses. These stiffness values can be seen below.

$$[A]_{ij} = \sum_{k=1}^{N} \left[\overline{Q_{ij}}\right]_k (z_k - z_{k-1})$$

$$[B]_{ij} = \frac{1}{2} \sum_{k=1}^{N} \left[\overline{Q_{ij}}\right]_k (z_k^2 - z_{k-1}^2) \tag{2.22}$$

$$[D]_{ij} = \frac{1}{3} \sum_{k=1}^{N} \left[\overline{Q_{ij}}\right]_k (z_k^3 - z_{k-1}^3) = \sum_{k=1}^{N} \left[\overline{Q_{ij}}\right]_k \left(t_k \bar{z}_k^2 - \frac{t_k^3}{12}\right) \qquad i,j = 1,2,6$$

The thickness of the layer is represented by t_k, and the length from the middle plane to the center of the layer is given by $\overline{z_k}$.

The B_{ij} coefficients provide a coupling between flexion and extension at the plate during transverse displacements. In the case of symmetric laminates, the coupling stiffnesses B_{ij}, D_{16}, and D_{26} are considered to be zero.

2.3. Governing Differential Equations

If we examine a plate exposed due to pressure components (P_x , P_y , q) and in-plane stress resultants (N_x , N_y , N_{xy}), we can obtain force-moment equilibrium on an infinitesimal plate, and the summation of these forces at x, y, and z yields the following equations, respectively:

$$\frac{\partial N_x}{\partial x} + \frac{\partial N_{xy}}{\partial y} - Q_x \frac{\partial w}{\partial x} + P_x = 0$$

$$\frac{\partial N_{xy}}{\partial x} + \frac{\partial N_y}{\partial y} - Q_y \frac{\partial w}{\partial y} + P_y = 0 \tag{2.23}$$

$$\frac{\partial Q_x}{\partial x} + \frac{\partial Q_y}{\partial y} + N_x \frac{\partial^2 w}{\partial x^2} + 2N_{xy} \frac{\partial^2 w}{\partial x \partial y} + N_y \frac{\partial^2 w}{\partial y^2} + q = 0$$

By combining the moments in the x and y directions, we can obtain the subsequent equations,

$$Q_x = \frac{\partial M_x}{\partial x} + \frac{\partial M_{xy}}{\partial y}$$

$$Q_y = \frac{\partial M_{xy}}{\partial x} + \frac{\partial M_y}{\partial y} \tag{2.24}$$

Since the transverse shear forces Q_x , Q_y and slopes $\frac{\partial w}{\partial x}$, $\frac{\partial w}{\partial y}$ are small, Eq. (2.23) and Eq. (2.24) may be expressed the following way,

$$\frac{\partial N_x}{\partial x} + \frac{\partial N_{xy}}{\partial y} + P_x = 0$$

$$\frac{\partial N_{xy}}{\partial x} + \frac{\partial N_y}{\partial y} + P_y = 0 \tag{2.25}$$

$$\frac{\partial^2 M_x}{\partial x^2} + 2\frac{\partial^2 M_{xy}}{\partial x \partial y} + \frac{\partial^2 M_y}{\partial y^2} + N_x \frac{\partial^2 w}{\partial x^2} + 2N_{xy} \frac{\partial^2 w}{\partial x \partial y} + N_y \frac{\partial^2 w}{\partial y^2} + q = 0$$

Eq. (2.25) can be considered in two parts, except for w and body force. The initial part of these is the onset of buckling, which is indicated by "i", and the other piece is the buckling, which is indicated by "b".

$$N_x = N_x^i + N_x^b$$

$$M_x = M_x^i + M_x^b \tag{2.26}$$

Prior to buckling, the plate is regarded to be flat. Thus,

$$w = w^b \tag{2.27}$$

It is believed that no further body force is applied during the buckling.

$$P_x = P_x^i\,, \qquad P_y = P_y^i\,, \qquad q = q^i \tag{2.28}$$

At the onset of buckling, Eq. (2.25) might be expressed in the following form:

$$\frac{\partial N_x^i}{\partial x} + \frac{\partial N_{xy}^i}{\partial y} + P_x^{,i} = 0$$

$$\frac{\partial N_{xy}^i}{\partial x} + \frac{\partial N_y^i}{\partial y} + P_y^i = 0 \tag{2.29}$$

$$\frac{\partial^2 M_x^i}{\partial x^2} + 2\frac{\partial^2 M_{xy}^i}{\partial x \partial y} + \frac{\partial^2 M_y^i}{\partial y^2} + q^i = 0$$

The following equations are obtained by substituting Eq. (2.26), (2.27), and (2.28) in Eq. (2.25) and subtracting Eq. (2.29).

$$\frac{\partial N_x^b}{\partial x} + \frac{\partial N_{xy}^b}{\partial y} = 0$$

$$\frac{\partial N_{xy}^b}{\partial x} + \frac{\partial N_y^b}{\partial y} = 0$$

$$\frac{\partial^2 M_x^b}{\partial x^2} + 2\frac{\partial^2 M_{xy}^b}{\partial x \partial y} + \frac{\partial^2 M_y^b}{\partial y^2} + N_x^i \frac{\partial^2 w}{\partial x^2} + 2N_{xy}^i \frac{\partial^2 w}{\partial x \partial y} + N_y^i \frac{\partial^2 w}{\partial y^2} = 0 \tag{2.30}$$

And the following three terms

$$N_x^b \frac{\partial^2 w}{\partial x^2} + 2N_{xy}^b \frac{\partial^2 w}{\partial x \partial y} + N_y^b \frac{\partial^2 w}{\partial y^2} \tag{2.31}$$

are regarded as minor in comparison to the previous three terms of the third term of Eq. (2.30) and have been omitted from it. Eq. (2.31) has three non-linear components N_x, N_y, and N_{xy} are functions of w. These parameters should be discarded if the buckling problem is to be considered reasonable and feasible. Since $w^i = 0$, then $K_x^i = K_y^i = K_{xy}^i = 0$. Substituting Eq. (2.4) and (2.8) into (2.29) yields,

$$\frac{\partial}{\partial x}\left[A_{11}\frac{\partial u^i}{\partial x} + A_{12}\frac{\partial v^i}{\partial y} + A_{16}\left(\frac{\partial v^i}{\partial x} + \frac{\partial u^i}{\partial y}\right)\right] + \frac{\partial}{\partial y}\left[A_{16}\frac{\partial u^i}{\partial x} + A_{26}\frac{\partial v^i}{\partial y} + A_{66}\left(\frac{\partial v^i}{\partial x} + \frac{\partial u^i}{\partial y}\right)\right] + P_x^i = 0 \tag{2.32.a}$$

$$\frac{\partial}{\partial x}\left[A_{16}\frac{\partial u^i}{\partial x} + A_{26}\frac{\partial v^i}{\partial y} + A_{66}\left(\frac{\partial v^i}{\partial x} + \frac{\partial u^i}{\partial y}\right)\right] + \frac{\partial}{\partial y}\left[A_{12}\frac{\partial u^i}{\partial x} + A_{22}\frac{\partial v^i}{\partial y} + A_{26}\left(\frac{\partial v^i}{\partial x} + \frac{\partial u^i}{\partial y}\right)\right] + P_y^i = 0 \tag{2.32.b}$$

$$\frac{\partial^2}{\partial x^2}\left[B_{11}\frac{\partial u^i}{\partial x} + B_{12}\frac{\partial v^i}{\partial y} + B_{16}\left(\frac{\partial v^i}{\partial x} + \frac{\partial u^i}{\partial y}\right)\right] + 2\frac{\partial^2}{\partial x \partial y}\left[B_{16}\frac{\partial u^i}{\partial x} + B_{26}\frac{\partial v^i}{\partial y} + B_{66}\left(\frac{\partial v^i}{\partial x} + \frac{\partial u^i}{\partial y}\right)\right] + \frac{\partial^2}{\partial y^2}\left[B_{12}\frac{\partial u^i}{\partial x} + B_{22}\frac{\partial v^i}{\partial y} + B_{26}\left(\frac{\partial v^i}{\partial x} + \frac{\partial u^i}{\partial y}\right)\right] + q^i = 0 \tag{2.32.c}$$

The subscript "o" has been deleted from the displacements for clarity. As mentioned before, the B_{ij} term is "zero" for a symmetrically laminated plate. Then the Eq. (2.32.c) yields $q^i = 0$.

The three parts of in-plane displacement may be used to conveniently illustrate the equilibrium equations governing the buckled configuration. If Eq. (2.4), Eq (2.5), and Eq. (2.9) are placed in Eq. (2.30), a matrix like the one below is obtained.

$$\begin{bmatrix} L_{11} & L_{12} & L_{13} \\ L_{21} & L_{22} & L_{23} \\ L_{31} & L_{32} & (L_{33} - F) \end{bmatrix} \begin{Bmatrix} u \\ v \\ w \end{Bmatrix} = \begin{Bmatrix} 0 \\ 0 \\ 0 \end{Bmatrix} \tag{2.33}$$

The differential operators identified as L_{ij} determine the plate's rigidity. These operators are in charge of measuring stiffness.

$$L_{11} \equiv A_{11}\frac{\partial^2}{\partial x^2} + 2A_{16}\frac{\partial^2}{\partial x \partial y} + A_{66}\frac{\partial^2}{\partial y^2}$$

$$L_{22} \equiv A_{22}\frac{\partial^2}{\partial y^2} + 2A_{26}\frac{\partial^2}{\partial x \partial y} + A_{66}\frac{\partial^2}{\partial x^2}$$

$$L_{33} \equiv D_{11}\frac{\partial^4}{\partial x^4} + 4D_{16}\frac{\partial^4}{\partial x^3 \partial y} + 2(D_{12} + 2D_{66})\frac{\partial^4}{\partial x^2 \partial y^2} + 4D_{26}\frac{\partial^4}{\partial x \partial y^3} + D_{22}\frac{\partial^4}{\partial y^4} \tag{2.34}$$

$$L_{12} = L_{21} \equiv A_{16}\frac{\partial^2}{\partial x^2} + (A_{12} + A_{66})\frac{\partial^2}{\partial x \partial y} + A_{26}\frac{\partial^2}{\partial y^2}$$

$$L_{13} = L_{31} \equiv -B_{11}\frac{\partial^3}{\partial x^3} - 3B_{16}\frac{\partial^3}{\partial x^2 \partial y} - (B_{12} + 2B_{66})\frac{\partial^3}{\partial x \partial y^2} - B_{26}\frac{\partial^3}{\partial y^3}$$

$$L_{23} = L_{32} \equiv -B_{16}\frac{\partial^3}{\partial x^3} - (B_{12} - 2B_{66})\frac{\partial^3}{\partial x^2 \partial y} - 3B_{26}\frac{\partial^3}{\partial x \partial y^2} - B_{22}\frac{\partial^3}{\partial y^3}$$

The differential operator F indicates the in-plane loading.

$$F \equiv N_x\frac{\partial^2}{\partial x^2} + 2N_{xy}\frac{\partial^2}{\partial x \partial y} + N_y\frac{\partial^2}{\partial y^2} \tag{2.35}$$

For the sake of straightforwardness, the characters "b" and "i" are omitted in Eq. (2.30).

In the sections that follow and the main body of the work, it will be assumed that N_x, N_{xy}, and N_y stand in for the inplane forces that exist right before buckling occurs, while u, v, and w reflect the plate's tiny displacements throughout buckling.

Since B_{ij} is equal to zero in symmetrically laminated plates, as was previously noted, in Eq. (2.33), L_{13} and L_{23} result in zero. Eq. (2.33) thus distinguishes between the in-plane and transverse parts of the issue. The in-plane portion of the buckled configuration results in $u = v = 0$ and the transverse displacements are governed by:

$$D_{11}\frac{\partial^4 w}{\partial x^4} + 4D_{16}\frac{\partial^4 w}{\partial x^3 \partial y} + 2(D_{12} + 2D_{66})\frac{\partial^4 w}{\partial x^2 \partial y^2} + 4D_{26}\frac{\partial^4 w}{\partial x \partial y^3} + D_{22}\frac{\partial^4 w}{\partial y^4} = N_x\frac{\partial^2 w}{\partial x^2} + 2N_{xy}\frac{\partial^2 w}{\partial x \partial y} + N_y\frac{\partial^2 w}{\partial y^2} \tag{2.36}$$

Eq. (2.36) is identical to the buckling equation for a homogeneous and anisotropic plate, with the exception of the technique used to get the stiffness coefficients D_{ij}.

When the ply above the midplane is the same orientation as the ply below the midplane in symmetrical laminated cross-ply plates, There is no connection or influence between the bending and twisting of an object. Due to the lack of coupling, $D_{12} = D_{16} = 0$. Eq. (2.37) can be derived by changing Eq. (2.36). The equation explained depicts the buckling phenomenon in a homogeneous orthotropic plate.

$$D_{11}\frac{\partial^4 w}{\partial x^4} + 2(D_{12} + 2D_{66})\frac{\partial^4 w}{\partial x^2 \partial y^2} + D_{22}\frac{\partial^4 w}{\partial y^4} = N_x\frac{\partial^2 w}{\partial x^2} + 2N_{xy}\frac{\partial^2 w}{\partial x \partial y} + N_y\frac{\partial^2 w}{\partial y^2} \tag{2.37}$$

2.4. Boundary Conditions

If a plate whose boundary condition is simply supported (SSSS) on each side and whose edge lengths a and b, thickness h is considered as in Figure 2.7, the equations formed due to the boundary conditions will be as in equation (2.38).

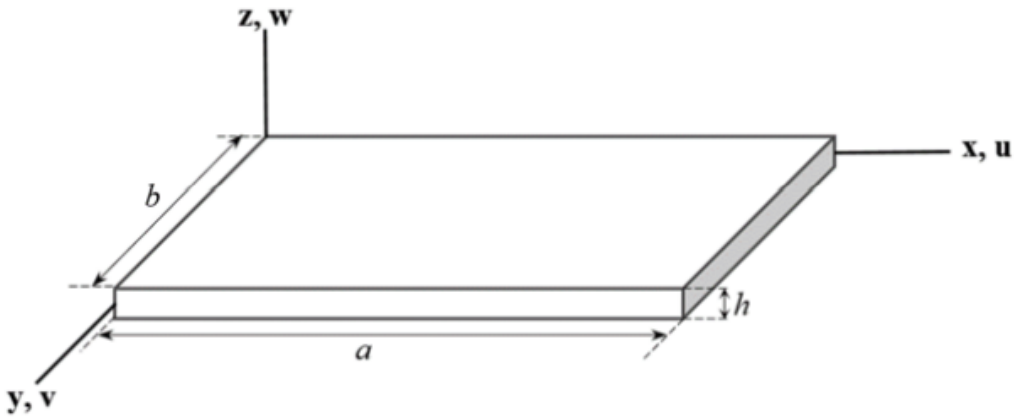

Figure 2.7. Geometry of the Plate.

$$\begin{aligned} &x = 0; && w(0,y) = 0; && M_x(0,y) = 0 \\ &x = a; && w(a,y) = 0; && M_x(a,y) = 0 \\ &y = 0; && w(x,0) = 0; && M_y(x,0) = 0 \\ &y = b; && w(x,b) = 0; && M_y(x,b) = 0 \end{aligned} \tag{2.38}$$

The bending moments have been designated by M_x and M_y, while the out-of-plane deflection of the plate's surface can be represented by w. Moments are,

$$M_x = -\left(D_{11}\frac{\partial^2 w}{\partial x^2} + D_{12}\frac{\partial^2 w}{\partial y^2}\right)$$

$$M_y = -\left(D_{12}\frac{\partial^2 w}{\partial x^2} + D_{22}\frac{\partial^2 w}{\partial y^2}\right) \tag{2.39}$$

$$M_{xy} = -2D_{66}\frac{\partial^2 w}{\partial x \partial y}$$

N_{xy} and N_y in Eq. (2.37) are equal to zero if a plate is solely exposed to axial compressive load per unit width, as can be observed in Figure 2.8.

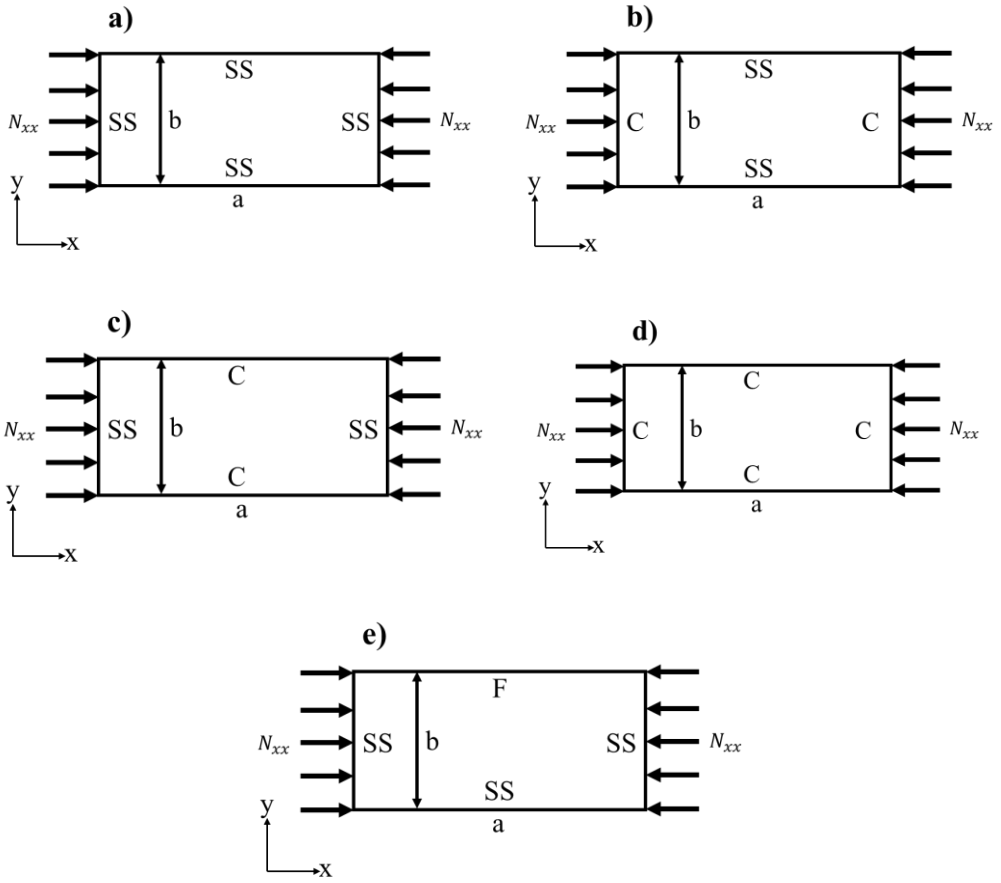

Figure 2.8. Composite Laminate under Uniaxial Compression, (a) SSSS, (b) CCSS, (c) SSCC, (d) CCCC, (e) SSSF.

Adjusting the mode shapes to the following will unquestionably fulfil the boundary criteria indicated in Eq. (2.38):

$$w_{mn} = C_{mn} \sin\left(\frac{m\pi x}{a}\right) \sin\left(\frac{n\pi x}{a}\right) \qquad m, n = 1,2,3 \ldots \tag{2.40}$$

The quantity of half-waves in both directions of x and y is denoted by m and n. C_{mn} is an arbitrary amplitude parameter with a tiny amount of value. If the constraints on the boundary are simply supported on each edge (SSSS) of a plate, the load that's critical can be calculated using Eq. (2.37).

$$(N_{xx})_{cr} = \pi^2 \left[D_{11} \left(\frac{m}{a}\right)^2 + 2(D_{12} + 2D_{66}) \left(\frac{n}{b}\right)^2 \left(\frac{a}{m}\right)^2 \right] \tag{2.41}$$

Besides the SSSS condition, Kassapoglou obtained critical buckling loads for different boundary conditions [17].

The critical buckling load (CCSS) for plate (b) can be seen in Figure 2.8 is as in Eq. (2.42).

$$\lambda = \frac{a}{b}\left(\frac{D_{22}}{D_{11}}\right)^{\frac{1}{4}}$$

$$K = \frac{4}{\lambda^2} + \frac{2(D_{12} + 2D_{66})}{\sqrt{D_{11}D_{22}}} + \frac{3}{4}\lambda^2 \quad , 0 < \lambda < 1.662$$

$$K = \frac{m^4 + 8m^2 + 1}{\lambda^2(m^2 + 1)} + \frac{2(D_{12} + D_{66})}{\sqrt{D_{11}D_{22}}} + \frac{\lambda^2}{m^2 + 1} \quad , \lambda > 1.662 \tag{2.42}$$

$$(N_{xx})_{cr} = \frac{\pi^2}{b^2}\sqrt{D_{11}D_{22}}(K)$$

The critical buckling load (SSCC) for the plate (c) in Figure 2.8 is,

$$\lambda = \frac{a}{b}\left(\frac{D_{22}}{D_{11}}\right)^{\frac{1}{4}}$$

$$K = \frac{m^2}{\lambda^2} + \frac{2(D_{12} + 2D_{66})}{\sqrt{D_{11}D_{22}}} + \frac{16\lambda^2}{3m^2} \tag{2.43}$$

$$(N_{xx})_{cr} = \frac{\pi^2}{b^2}\sqrt{D_{11}D_{22}}(K)$$

Figure 2.8 shows the critical load that causes buckling (CCCC) for the (d), which is,

$$\lambda = \frac{a}{b}\left(\frac{D_{22}}{D_{11}}\right)^{\frac{1}{4}}$$

$$K = \frac{4}{\lambda^2} + \frac{8(D_{12} + 2D_{66})}{3\sqrt{D_{11}D_{22}}} + 4\lambda^2 \quad , 0 < \lambda < 1.094$$

$$K = \frac{m^4 + 8m^2 + 1}{\lambda^2(m^2 + 1)} + \frac{2(D_{12} + D_{66})}{\sqrt{D_{11}D_{22}}} + \frac{\lambda^2}{m^2 + 1} \quad , \lambda > 1.094 \tag{2.44}$$

$$(N_{xx})_{cr} = \frac{\pi^2}{b^2}\sqrt{D_{11}D_{22}}(K)$$

Figure 2.8 shows the critical load that causes buckling (SSSF) for the (e), which is,

$$\lambda = \frac{a}{b}\left(\frac{D_{22}}{D_{11}}\right)^{\frac{1}{4}}$$

$$K = \frac{12}{\pi^2} + \frac{D_{66}}{\sqrt{D_{11}D_{22}}} + \frac{1}{\lambda^2} \tag{2.45}$$

$$(N_{xx})_{cr} = \frac{\pi^2}{b^2}\sqrt{D_{11}D_{22}}(K)$$

3. Mixing and Material Properties

3.1. Introduction

The Young's modulus of a material is determined using the following techniques: the Rule of Mixtures and Halpin-Tsai. When evaluating the mechanical characteristics of a material, the Rule of Mixtures and Halpin-Tsai techniques are frequently used. The Rule of Mixtures technique establishes the mechanical features of a material by calculating the proportions of its components. This method derives a composite material's elastic modulus of elasticity by the addition of the moduli of elasticity of the different components in proportion to their respective ratios within the composite. In contrast, the Halpin-Tsai method provides a more comprehensive approach to estimating the mechanical characteristics of a material. When estimating the mechanical characteristics of a material, this method considers aspects such as the proportion of components, mechanical characteristics, and component interactions. In this way, the Halpin-Tsai method gives more accurate results and is a more sensitive method than the Rule of Mixtures method. Figure 3.1 shows a composite laminate containing carbon nanotubes.

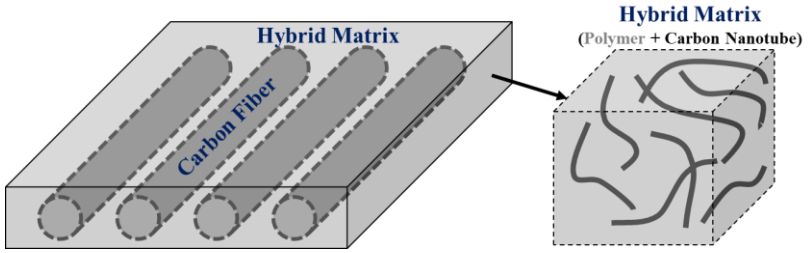

Figure 3.1. Unidirectional Fiber Reinforced Composite Lamina Containing CNT.

3.2. Mixing Equations

The modulus of elasticity of a CNT reinforced resin is obtained using the Halpin-Tsai model.

$$E_{m-cnt} = E_m \left(\frac{1 + 2R\delta V_{cnt}}{1 - \delta V_{cnt}} \right) \tag{3.1}$$

where R and δ values are defined as in the equations below.

$$R = \frac{L_{cnt}}{d_{cnt}} \tag{3.2}$$

$$\delta = \frac{\frac{E_{cnt}}{E_m} - 1}{\frac{E_{cnt}}{E_m} + 2R} \tag{3.3}$$

where E_m represents the modulus of elasticity of the polymer resin, E_{cnt} the modulus of elasticity of CNT, V_{cnt} the volume fraction of CNT, d_{cnt} the mean outer diameter of the nanotube, and L_{cnt} the length of the nanotube.

The Halpin-Tsai (H-T) model in Eq. (3.1) predicts the elastic modulus of straight-aligned CNT-reinforced nanocomposites under the assumption that CNTs are distributed uniformly throughout the polymer matrix. Since CNTs are not always precisely aligned in nature, it is quite challenging to uniformly distribute CNTs throughout the polymer matrix. In such circumstances, Eq. (3.3) is no longer accurate [24]. Considerations for this study include orientation, waviness, and agglomeration. The updated Halpin-Tsai model must take them into account. Rearranging Eq. (3.3) results in Eq. (3.4).

$$\delta = \frac{f_R f_W f_A \frac{E_{cnt}}{E_m} - 1}{f_R f_W f_A \frac{E_{cnt}}{E_m} + 2R} \tag{3.4}$$

First, f_R is included to calculate the random orientation of the CNTs, and this is the orientation factor. When its length is much smaller than the sample thickness, it is assumed to be randomly oriented in three dimensions and is taken as $f_R = \frac{1}{6}$. If the length of the CNT is greater than the thickness of the sample, it is assumed that it is randomly oriented in two dimensions and is taken as $f_R = \frac{1}{3}$ [24]. In this study, f_R will be taken as $\frac{1}{6}$.

Then, the f_W waviness factor is taken into account. f_W is discovered as in Eq. (3.5). It can be assumed as $f_W = 0.6$.

$$f_W = 1 - \frac{A}{W} \tag{3.5}$$

where W is the half wavelength, and A is the amplitude. The schematic illustration resembles Figure 3.2.

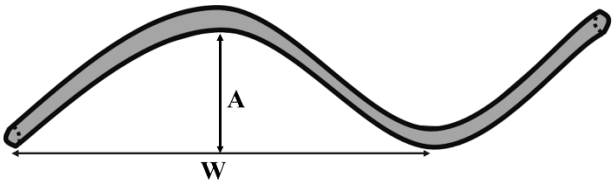

Figure 3.2. Schematic Illustration of a Curved CNT.

Finally, the agglomeration efficiency factor, f_A, is included. The f_A value can be found as in Eq. (3.6).

$$f_A = e^{-\alpha V_{cnt}^{\beta}} \tag{3.6}$$

The values of 10 and 0.9 might be assigned to α and β, respectively, and they are linked to the level of CNT agglomeration.

The shear modulus of a CNT-impregnated resin is found as in Eq. (3.7).

$$G_{m-cnt} = \frac{E_{m-cnt}}{2(v_{m-cnt} + 1)} \tag{3.7}$$

The ratio of Poisson's of pure resin and resin impregnated with CNTs can be deemed identical.

$$v_{m-cnt} = v_m \tag{3.8}$$

The density of the carbon nanotube-reinforced resin, resulting in the density of the composite lamina, can be calculated using the aforementioned formulae.

$$\rho_{m-cnt} = \rho_{cnt} V_{cnt} + \rho_m V_m \tag{3.9}$$

$$\rho_c = \rho_f V_f + \rho_{m-cnt} V_{m-cnt} \tag{3.10}$$

where subscript m is the matrix, subscript cnt is carbon nanotube, subscript f is fiber, and subscript m-cnt is matrix with CNT-reinforced. V stands for the volume fraction.

The technique of the rule of mixtures is used to find the modulus of elasticity of laminae in the direction of the longitudinal axis, as well as Poisson's number, using the formulae that are provided.

$$E_1 = E_f V_f + E_{m-cnt} V_{m-cnt} \tag{3.11}$$

$$v_{12} = v_f V_f + v_{m-cnt} V_{m-cnt} \tag{3.12}$$

In the aforementioned scenario, E_f symbolizes the fiber's elastic modulus, V_f denotes its volume fraction, and v_f represents the fiber's Poisson's ratio. For the purposes of this investigation, the fiber volume percentage is fixed at 60% and the matrix portion of volume at 40%.

The experimental findings show that the rule of mixtures technique falls short of satisfying the material properties (E_2, v_{23}, G_{12}, and G_{23}) in the transverse direction. The Halpin-Tsai technique is employed to assess the material characteristics in the transverse direction. The following is the Halpin-Tsai equation. [24]

$$P = P_{m-cnt}\left(\frac{1 + \xi \eta V_f}{1 - \eta V_f}\right) \tag{3.13}$$

In this case, P_{m-cnt} may represent any structural element of the CNT-reinforced matrix. The transverse moduli of elasticty E_2, the transverse ratio of Poisson's v_{23}, the in-plane shear moduli G_{12}, or the out-of-plane moduli of shear G_{23} are a few examples of properties of the composite lamina that P might be. The η is the experimental factor and can be explain as follows:

$$\eta = \frac{P - P_{m-cnt}}{P + \xi P_{m-cnt}} \tag{3.14}$$

The reinforcing factor in this case is called ξ, and it is dependent on the loading conditions, packing geometry, and fiber geometry. $\xi = 2$ is used to discover E_2, while $\xi = 1$ is used to find v_{23}, G_{12}, and G_{23} [32].

3.3. Material Properties of Carbon Nanotube Reinforced Composite Plates

The numbers utilized by Georgantzinos et al. [24] for material parameters in this investigation were chosen to permit an accurate juxtaposition of the CNT impact with the outcomes of previous studies. The table below provides a complete explanation of various material properties.

Table 3.1. Properties of the material of the fiber, matrix, and CNT.

Carbon Fiber AS4		**Epoxy Resin 3501-6**		**CNT**	
$E_{f_{11}}$ (GPa)	225	E_m (GPa)	4.2	E_{cnt} (GPa)	900
$E_{f_{22}}$ (GPa)	15	G_m (GPa)	1.567	L_{cnt} (nm)	2000
$G_{f_{12}}$ (GPa)	15	v_m	0.34	d_{cnt} (nm)	30
$G_{f_{23}}$ (GPa)	7	ρ_m (g/cm^3)	1.25	ρ_{cnt} (g/cm^3)	2.25
$v_{f_{12}}$	0.2				
$v_{f_{23}}$	0.4				
ρ_f (g/cm^3)	1.8				

While the laminate properties are described in depth in this study, the percentages of fibers and resin are accepted as 60% and 40%, respectively. These ratios were used to calculate the outcomes of the study.

3.3.1. Effect of the Waviness Factor on the Elastic Modulus

The waviness factor is taken into account using the CNT's half wavelength and amplitude. When wavelength and amplitude change, the waviness factor decreases or increases. In this study, the waviness factor was accepted as 0.6, but the effect on the elastic modulus for different values was observed as in the Figure 3.3 and Figure 3.4. The closer the waviness factor is to 1.0, the greater the elastic modulus. It shows the elastic modulus decreasing curve after a certain CNT volume fraction.

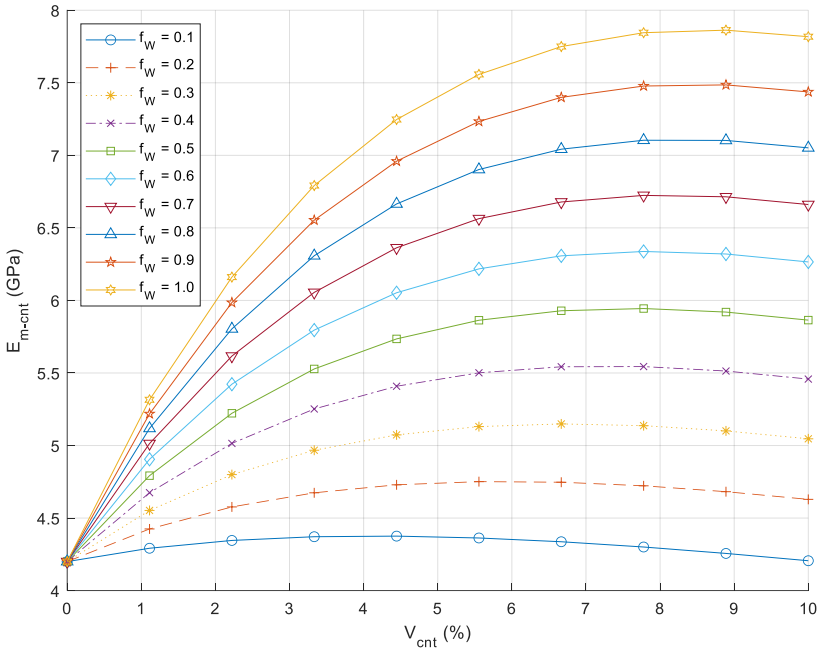

Figure 3.3. CNT Volume Fraction and Elastic Moduli of Matrix Reinforced with CNTs for Various Waviness Factors.

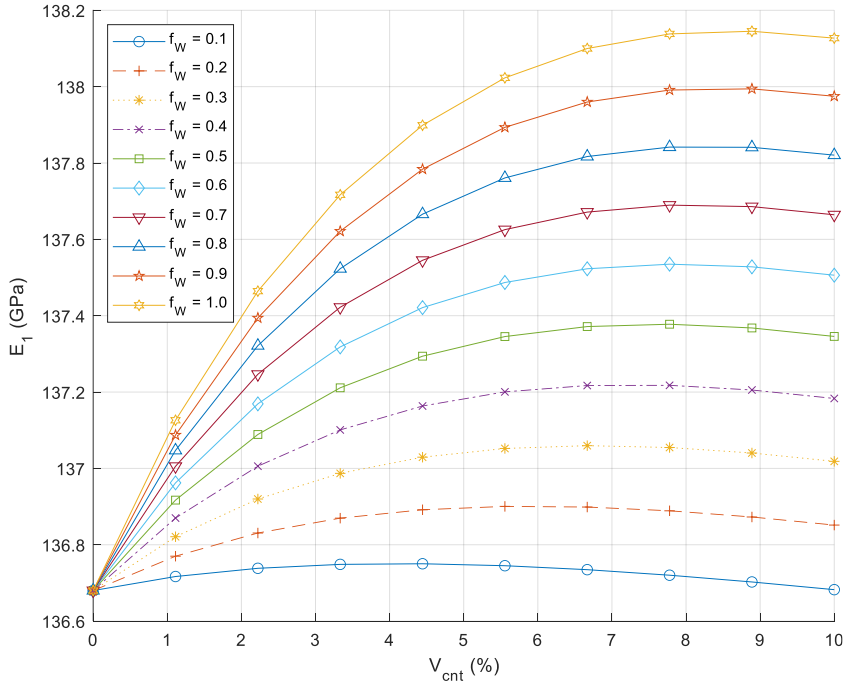

Figure 3.4. Volume Fraction of CNT and Elastic Moduli of Matrix Reinforced with CNTs for Various Waviness Factors.

3.3.2. Effect of Agglomeration on the Elastic Modulus

Figure 3.5 and Figure 3.6 display the findings of the examination of the response of the elastic modulus to the degree of agglomeration factor, which ranges from 0 to 15. The elastic modulus grows almost linearly when the degree of agglomeration factor is 0, but it falls as the degree of agglomeration factor increases. The agglomeration factor is inversely proportional to the degree of agglomeration factor. Consequently, the closer the agglomeration factor is to 1.0, the greater the effect on the Young's modulus. That is, the more homogeneously carbon nanotube is distributed in the resin, the greater the elastic modulus.

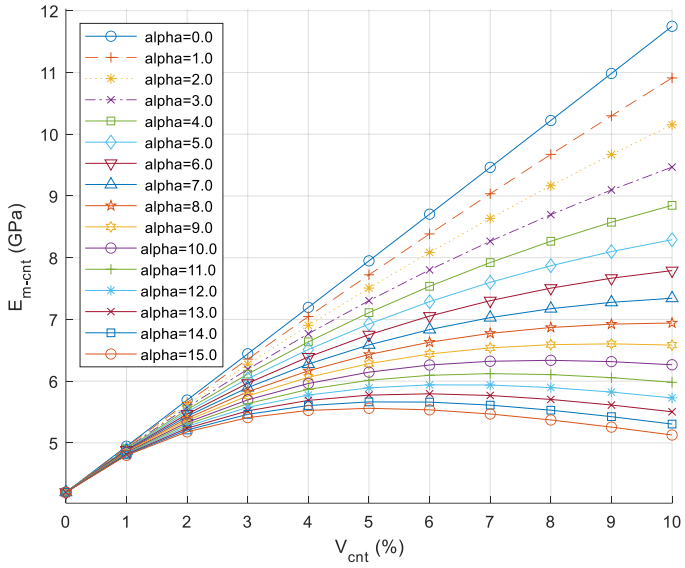

Figure 3.5. Volume Fraction of CNT and Elastic Modulus of CNT-Reinforced Matrix for Different Degree of Agglomeration Factors.

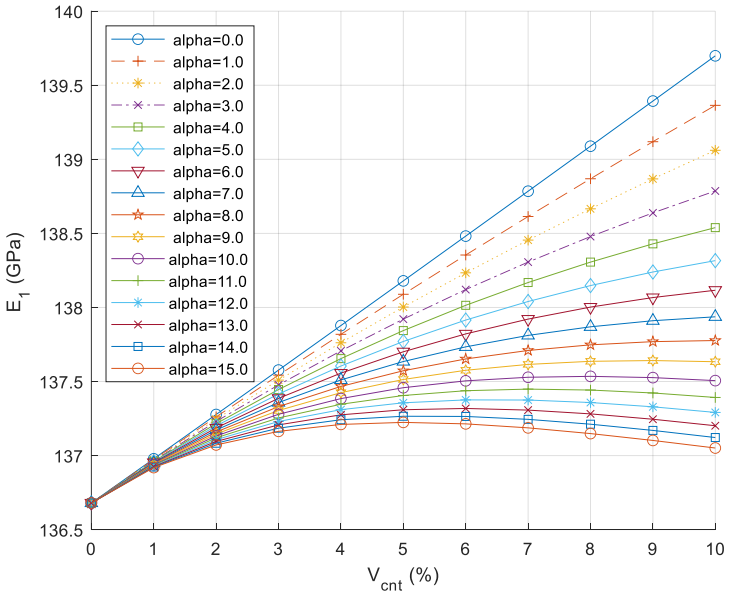

Figure 3.6. Volume Fraction of CNT and Elastic Moduli of Matrix Reinforced with CNTs for Various Degree of Agglomeration Factors.

3.3.3. Impact of CNT Volume Fraction on the Material Properties

Table 3.2 provides material properties according to various volume fractions of CNTs. As demonstrated, when the CNT fraction rises, consequently the elastic and shear modulus decrease. However, the amounts start reducing after a certain rate. As a result, an excess of CNT percentage growth can have detrimental impact on material characteristics.

Table 3.2. Laminate Material Properties for Various Volume Fraction of CNT.

V_{cnt} (%)	E_1 (GPa)	E_2 (GPa)	G_{12} (GPa)	G_{23} (GPa)	v_{12}
0	136.6800	9.0255	4.5365	3.4922	0.256
1	136.9376	9.6063	5.0255	3.7861	0.256
2	137.1327	10.0033	5.3718	3.9887	0.256
3	137.2788	10.2807	5.6190	4.1308	0.256
4	137.3849	10.4732	5.7924	4.2293	0.256
5	137.4582	10.6021	5.9095	4.2953	0.256
6	137.5046	10.6820	5.9823	4.3362	0.256
7	137.5288	10.7233	6.0200	4.3573	0.256
8	137.5350	10.7337	6.0295	4.3626	0.256
9	137.5264	10.7193	6.0163	4.3552	0.256
10	137.5061	10.6846	5.9846	4.3375	0.256

3.3.4. Effect of Volume Fraction of CNT on the D Matrix

The study investigated how the volume fraction of CNT affects the D matrix. The laminate was created using 8 plies at 0 degrees, represented as [0/0/0/0/0/0/0/0]. The investigation analyzed the changes in the D matrix of the laminate with varying volume fractions of CNT.

As indicated by the data presented in the Table 3.3, the values in the D matrix increase with the increase in CNT volume fraction. This increase in D matrix values has a positive effect on the material properties, particularly on the critical buckling load, which increases as well. However, if the CNT volume fraction is taken in excess, the values in the D matrix decrease, leading to a reduction in the critical buckling load.

In conclusion, properly adjusting the volume fraction of CNT can enhance material properties, especially the critical buckling load. However, an excessive increase in this fraction can adversely affect material properties. Therefore, careful control of the CNT volume fraction is crucial in material design.

Table 3.3. Effect of Volume Fraction of CNT on the D Matrix.

V_{cnt} (%)	D_{11} [N*mm]	$\Delta_{D_{11}}$ (%)	D_{12} [N*mm]	$\Delta_{D_{12}}$ (%)	D_{22} [N*mm]	$\Delta_{D_{22}}$ (%)	D_{66} [N*mm]	$\Delta_{D_{66}}$ (%)
0	11997.43	0.00	202.81	0.00	792.24	0.00	396.48	0.00
1	12023.31	0.22	215.92	6.46	843.45	6.46	439.21	10.78
2	12042.65	0.38	224.89	10.88	878.46	10.88	469.49	18.41
3	12057.02	0.50	231.15	13.97	902.94	13.97	491.09	23.86
4	12067.41	0.58	235.50	16.12	919.93	16.12	506.25	27.68
5	12074.57	0.64	238.42	17.55	931.31	17.55	516.47	30.26
6	12079.08	0.68	240.22	18.44	938.36	18.44	522.84	31.87
7	12081.43	0.70	241.15	18.90	942.01	18.90	526.13	32.70
8	12082.03	0.71	241.39	19.02	942.93	19.02	526.96	32.91
9	12081.20	0.70	241.06	18.86	941.65	18.86	525.81	32.62
10	12079.23	0.68	240.28	18.47	938.59	18.47	523.04	31.92

The modifications in D matrix values, impacted by changes in the volume fraction of CNT, are visually depicted in the Figure 3.7. These graphical representations offer a clear way to monitor the evolution of the D matrix as the CNT volume fraction is altered.

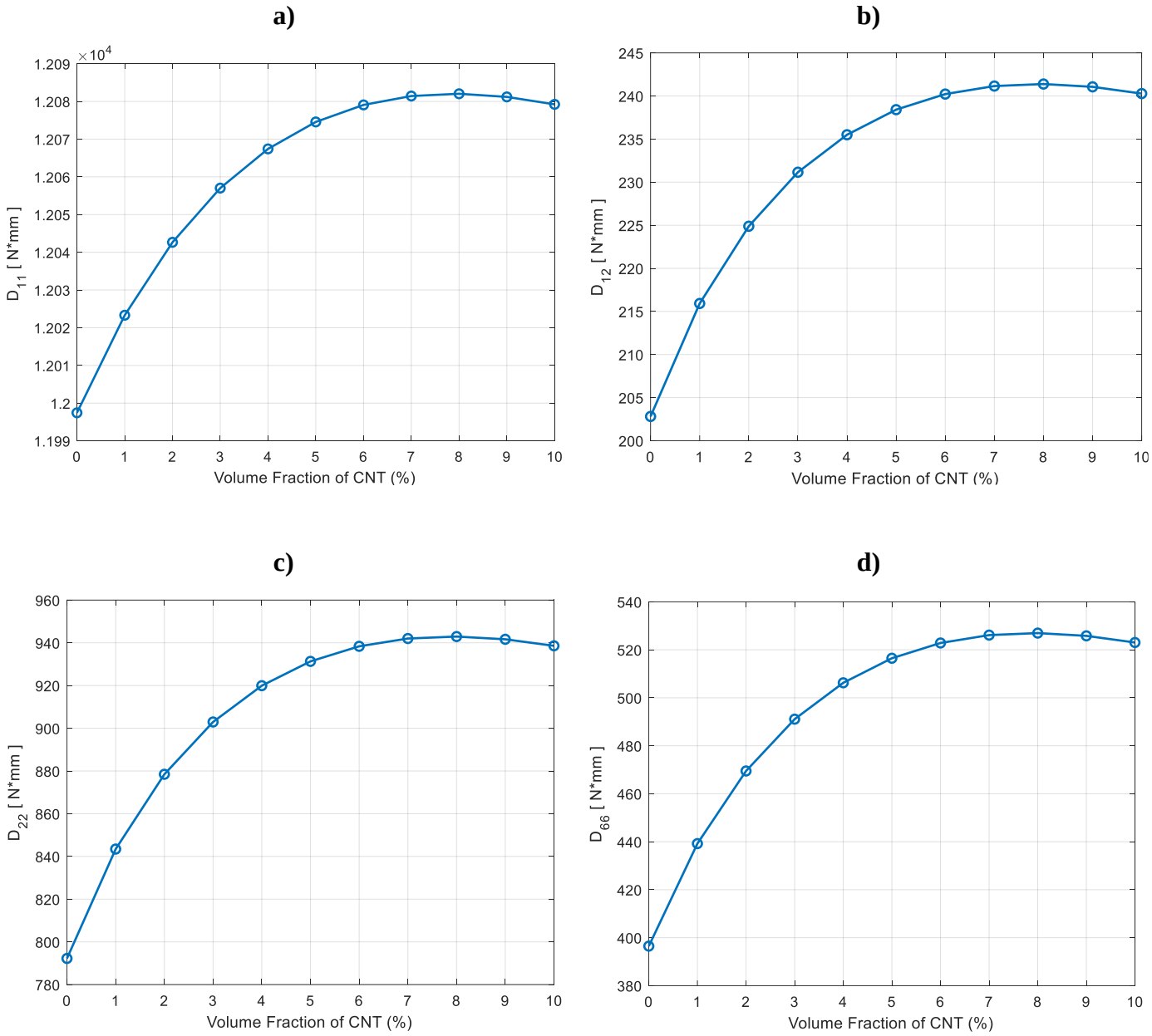

Figure 3.7. CNT Volume Fraction vs D Matrix (a) D_{11}, (b) D_{12}, (c) D_{22}, (d) D_{66}.

4. Calculation of Critical Buckling Load For a Composite Plate Without Hole

In this section, a plate with a long side (a) of 200 mm and a short side (b) of 100 mm was considered. An 8-ply laminate with properties specified in Table 3.1 was used. Both analytical and numerical (Finite Element Method) values were obtained and examined for verification. To improve the accuracy of results in the finite element model and minimize computational time, a mesh convergence study, also known as a mesh independence study, was conducted. The results obtained were compared within themselves and against the literature studies to ensure their accuracy. $\theta = 0°$ shows fiber orientations are perpendicular to applied load and $\theta = 90°$ indicates fiber orientations are parallel to the applied load.

4.1. Finite Element Model and Boundary Conditions

The FEM model was set up with an a/b ratio of 2 and a mesh size of 2 mm after conducting a mesh convergence study. The total number of elements in the mesh was 5000. Figure 4.1 illustrates the load and boundary conditions applied in the Simply Supported and Clamped Boundary Conditions in the FEM model.

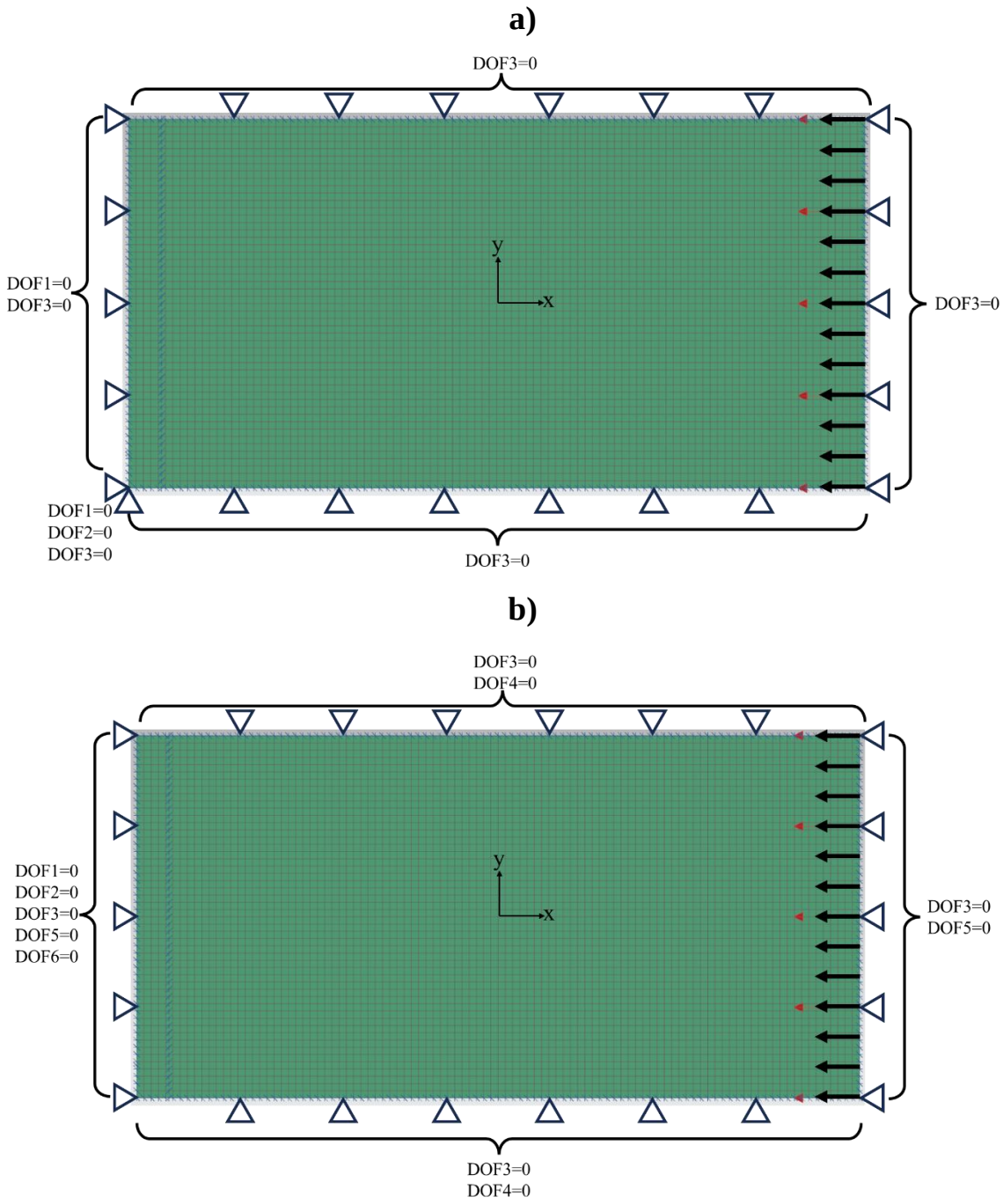

Figure 4.1. Finite Element Model and Boundary Conditions (a) SSSS and (b) CCCC.

In this study, parametric analysis was done with Simply Supported Boundary Condition. The QUAD4 element in NASTRAN was used as the shell element. It is generally used in modeling simple geometries. The QUAD4 element has 5 degrees-of-freedom (DOF) at each node. These are displacement in the x direction (DOF1), displacement in the y direction (DOF2), displacement in the z direction (DOF3), rotation in the x direction (DOF4) and rotation in the y direction (DOF5).

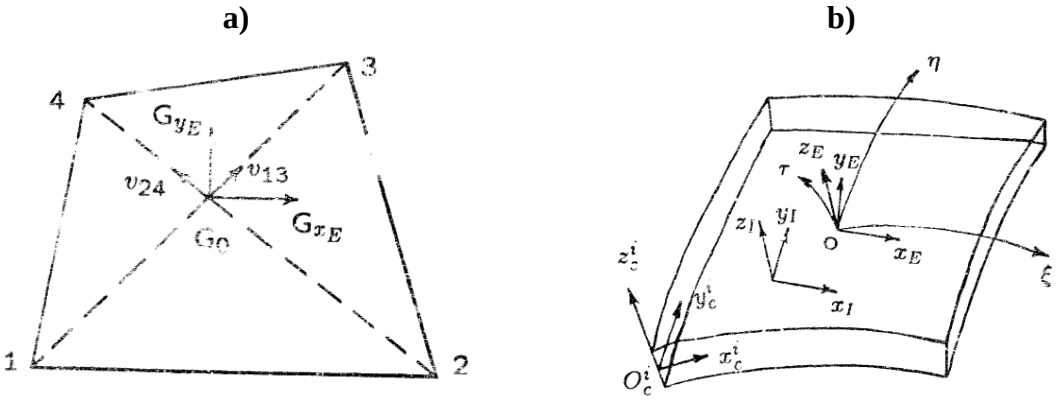

Figure 4.2. a) Element Coordinate System and b) Isoparametric Quadrilateral 4-Node Plate & Shell Element

$$\tilde{x}_E(\xi,\eta) = N_1\tilde{x}^1 + N_2\tilde{x}^2 + N_3\tilde{x}^3 + N_4\tilde{x}^4$$
$$\tilde{u}_E(\xi,\eta) = N_1\tilde{u}^1 + N_2\tilde{u}^2 + N_3\tilde{u}^3 + N_4\tilde{u}^4 \quad (4.1)$$

where $N_i(\xi,\eta)$ is shape functions, $\tilde{x}^i = [x_i,\ y_i,\ z_i]^t$ is grid point coordinates and $\tilde{u}^i = [u_i,\ v_i,\ w_i,\ \theta_{xi},\ \theta_{yi},\ \theta_{zi}]^t$ is grid point displacements.

Shape functions are,

$$N_i = \frac{1}{4}(1+\xi\xi_i)(1+\eta\eta_i)$$
$$\frac{\partial N_i}{\partial \xi} = \frac{1}{4}\xi_i(1+\eta\eta_i) \quad (4.2)$$
$$\frac{\partial N_i}{\partial \eta} = \frac{1}{4}\eta_i(1+\xi\xi_i)$$

Linear strain – displacement relations are,

$$\{\epsilon\} = \begin{pmatrix} \epsilon_x \\ \epsilon_y \\ \gamma_{xy} \\ \gamma_{yz} \\ \gamma_{zx} \end{pmatrix} = \begin{pmatrix} \dfrac{\partial u}{\partial x} \\ \dfrac{\partial v}{\partial y} \\ \dfrac{\partial u}{\partial y} + \dfrac{\partial v}{\partial x} \\ \dfrac{\partial w}{\partial y} + \dfrac{\partial v}{\partial z} \\ \dfrac{\partial w}{\partial x} + \dfrac{\partial u}{\partial z} \end{pmatrix} \tag{4.3}$$

Membrane – bending strain – displacement relations are,

$$\begin{pmatrix} \epsilon_M \\ \hline \epsilon_B \\ \hline \gamma_{TS} \end{pmatrix}_I = \left(\begin{array}{ccc|ccc} \dfrac{\partial N_i}{\partial x} & 0 & 0 & & & \\ 0 & \dfrac{\partial N_i}{\partial y} & 0 & & 0 & \\ \dfrac{\partial N_i}{\partial y} & \dfrac{\partial N_i}{\partial x} & 0 & & & \\ \hline & & & \dfrac{\partial N_i}{\partial x} & 0 & 0 \\ & 0 & & 0 & \dfrac{\partial N_i}{\partial y} & 0 \\ & & & \dfrac{\partial N_i}{\partial y} & \dfrac{\partial N_i}{\partial x} & 0 \\ \hline 0 & 0 & \dfrac{\partial N_i}{\partial y} & 0 & \dfrac{\partial N_i}{\partial z} & 0 \\ 0 & 0 & \dfrac{\partial N_i}{\partial x} & \dfrac{\partial N_i}{\partial z} & 0 & 0 \end{array}\right) \begin{pmatrix} u_M \\ v_M \\ w_M \\ \hline u_B \\ v_B \\ w_B \end{pmatrix}_I \tag{4.4}$$

Relation between $[u_m,\ v_m,\ w_m,\ u_b,\ v_b,\ w_b]$ and $[u,\ v,\ w,\ \theta_x,\ \theta_y,\ \theta_z]$ are,

$$\begin{pmatrix} u_M \\ v_M \\ w_M \\ u_B \\ v_B \\ w_B \end{pmatrix}_I = \left(\begin{array}{c|c} T & 0 \\ \hline 0 & \dfrac{Jt}{2}A \end{array}\right) \begin{pmatrix} u \\ v \\ w \\ \theta_x \\ \theta_y \\ \theta_z \end{pmatrix}_E \tag{4.5}$$

Jacobian (transformation from $\tilde{x}$ to $\tilde{\epsilon}$)

$$\begin{pmatrix} \frac{\partial N_i}{\partial \xi} \\ \frac{\partial N_i}{\partial \eta} \\ \frac{\partial N_i}{\partial \varsigma} \end{pmatrix} = \begin{pmatrix} \frac{\partial x}{\partial \xi} & \frac{\partial y}{\partial \xi} & \frac{\partial z}{\partial \xi} \\ \frac{\partial x}{\partial \eta} & \frac{\partial y}{\partial \eta} & \frac{\partial z}{\partial \eta} \\ \frac{\partial x}{\partial \varsigma} & \frac{\partial y}{\partial \varsigma} & \frac{\partial z}{\partial \varsigma} \end{pmatrix} \begin{pmatrix} \frac{\partial N_i}{\partial x} \\ \frac{\partial N_i}{\partial y} \\ \frac{\partial N_i}{\partial z} \end{pmatrix} \tag{4.6}$$

Stress and strain are related by,

$$\begin{pmatrix} \sigma_M \\ - \\ \sigma_B \\ - \\ \tau_{TS} \end{pmatrix} = \begin{pmatrix} G_1 & | & 0 & | & 0 \\ - & - & - & - & - \\ 0 & | & G_2 & | & 0 \\ - & - & - & - & - \\ 0 & | & 0 & | & G_3 \end{pmatrix} \begin{pmatrix} \sigma_M \\ - \\ \sigma_B \\ - \\ \gamma_{TS} \end{pmatrix} \tag{4.7}$$

Or

$$[\sigma]_I = [G]_I(\{\epsilon\})_I \tag{4.8}$$

where,

$\{\sigma_M\} - Membrane\ stress\ vector$

$\{\sigma_B\} - Bending\ stress\ vector$

$\{\tau_{TS}\} - Transverse\ shear\ stress\ vector$

$\{G_1\} - Membrane\ moduli\ matrix$

$\{G_2\} - Bending\ moduli\ matrix$

$\{G_3\} - Transverse\ shear\ moduli\ matrix$

$\{\epsilon_M\} - Membrane\ strain\ vector$

$\{\epsilon_B\} - Bending\ strain\ vector$

$\{\gamma_{TS}\} - Transverse\ shear\ strain\ vector$

Material constants transformation are,

$$[G]_I = [U]^T[G]_M[U] \tag{4.3}$$

Shape functions are defined in a normalized coordinate system (ξ, η) rather than the original (x, y) coordinate system. Isoparametric mapping can be seen in the figure below.

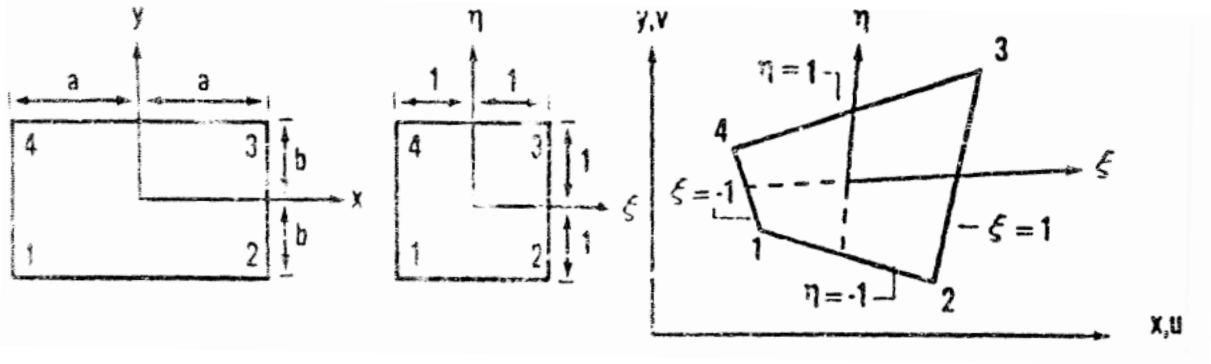

Figure 4.3. Isoparametric Mapping

where $\xi = \frac{x}{a}$ and $\eta = \frac{y}{b}$.

4.2. Mesh Convergence Study

As mentioned earlier, the mesh convergence study is a type of study that aims to evaluate the impact of mesh size on analysis results. In this study, the number of elements and the results were optimized while minimizing the calculation time. An 8-ply laminate consisting of 0 angle plies, i.e., [0/0/0/0/0/0/0/0], was used during the analysis. A 200 mm x 100 mm rectangular plate was used in the study, and the CNT volume fraction was taken as 0. The data obtained in the table below was obtained only for the fully simply supported case.

Table 4.1. Results of Mesh Convergence Study for SSSS Case.

Mesh Size [mm]	Critical Buckling Load [N/mm]
20	8.27
15	8.14
10	8.08
5	8.05
2	8.03
1	8.02

As can be seen from the results obtained, the values are very close to each other as the mesh size approaches 1 mm. As a result, a mesh size of 2 mm will be used in this study.

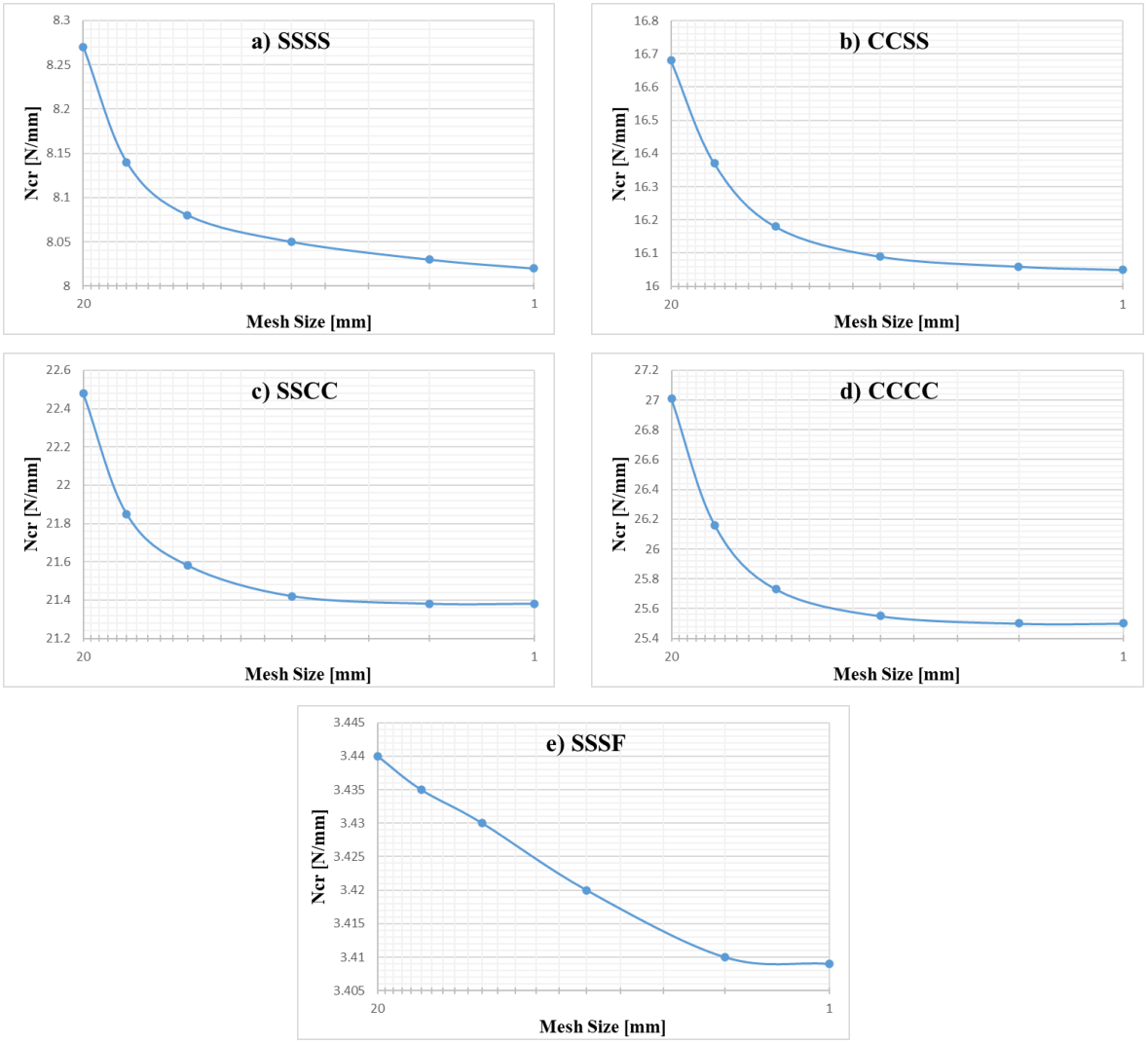

Figure 4.4. Graphical Results of Mesh Convergence Study (a) SSSS, (b) CCSS, (c) SSCC, (d) CCCC and (e) SSSF.

4.3. Effect of CNT Volume Fraction

Analyses of a 200 mm x 100 mm rectangular plate stacked as [0/0/0/0/0/0/0/0] were performed at different boundary conditions. Critical buckling loads at different CNT volume fractions were examined both numerically and analytically, and an error value was calculated from the results. Table 4.2 summarizes the derived analytical findings (using MATLAB). Table 4.3, on the other hand, shows the numerical outcomes (as calculated using FEM).

Table 4.2. Impact of CNT Volume Fraction on the Critical Buckling Load for Different Boundary Conditions (Analytical).

V_{cnt} (%)	$N_{cr_{SSSS}}$ [N/mm]	$N_{cr_{CCSS}}$ [N/mm]	$N_{cr_{SSCC}}$ [N/mm]	$N_{cr_{CCCC}}$ [N/mm]	$N_{cr_{SSSF}}$ [N/mm]
0	8.05	16.15	21.61	26.97	3.44
2	8.74	16.78	23.77	28.82	3.53
4	9.07	17.10	24.81	29.72	3.59
8	9.26	17.27	25.39	30.22	3.61
12	9.14	17.16	25.02	29.91	3.60

Table 4.3. Impact of CNT Volume Fraction on the Critical Buckling Load for Different Boundary Conditions (FEM).

V_{cnt} (%)	$N_{cr_{SSSS}}$ [N/mm]	$N_{cr_{CCSS}}$ [N/mm]	$N_{cr_{SSCC}}$ [N/mm]	$N_{cr_{CCCC}}$ [N/mm]	$N_{cr_{SSSF}}$ [N/mm]
0	8.03	16.06	21.38	25.50	3.41
2	8.71	16.68	23.54	27.08	3.51
4	9.04	16.99	24.58	27.84	3.56
8	9.23	17.17	25.16	28.20	3.59
12	9.11	17.06	24.79	28.00	3.57

Table 4.3 indicates that the critical threshold lowers as the CNT volume percentage increases. Apart from this, there is a negligible difference in the values obtained.

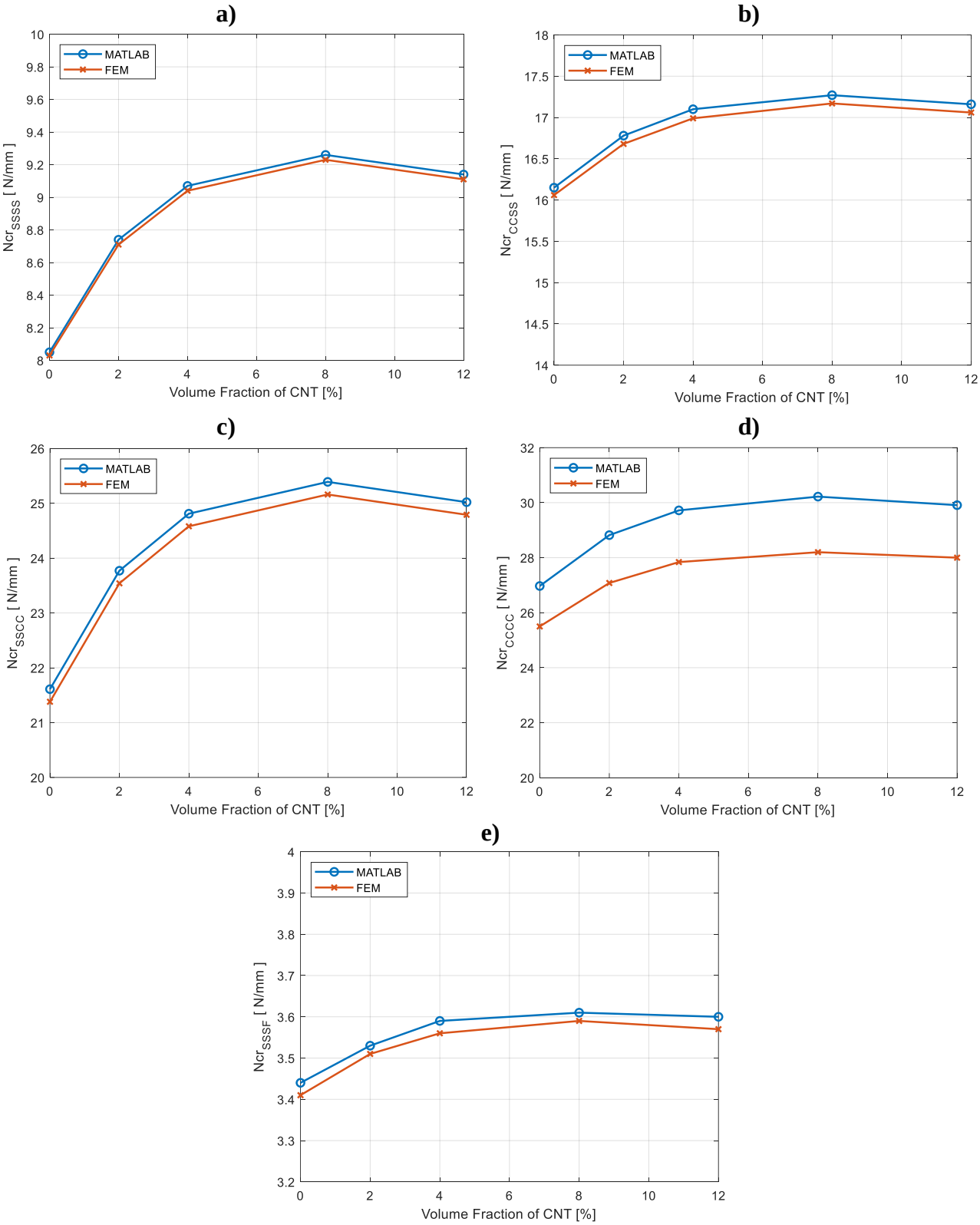

Figure 4.5. Impact of Volume Ratio of CNT on Critical Buckling Load for Different Boundary Constraints, (a) SSSS, (b) CCSS, (c) SSCC, (d) CCCC and (e) SSSF.

Table 4.4 presents the differences, i.e., error values, between numerical (Finite Element Method, FEM) and analytical solutions. These discrepancies arise from the presence of coupling terms of bending and twisting [B] within the stiffness [ABD] matrix [17]. Within this framework, the Finite Element Method proves to be advantageous in providing more accurate results compared to analytical approaches. This advantage stems from the fact that the analytical formulas used are often derived under specific assumptions or simplifications, which may not fully capture the complex behavior of the system [17]. On the contrary, the Finite Element Method incorporates and thoroughly answers these coupling issues, thereby offering a more realistic representation of the physical phenomena. It is important to note that the magnitude of the difference between analytical and numerical values is influenced by these factors, highlighting the necessity of using numerical methods in situations where analytical solutions may not adequately account for such complexities.

Table 4.4. Error Percentages of Critical Buckling Loads at Different Boundary Conditions.

V_{cnt} (%)	$\mathbf{Error_{SSSS}}$ (%)	$\mathbf{Error_{CCSS}}$ (%)	$\mathbf{Error_{SSCC}}$ (%)	$\mathbf{Error_{CCCC}}$ (%)	$\mathbf{Error_{SSSF}}$ (%)
0	0.29	0.57	1.05	5.46	0.76
2	0.31	0.62	0.95	6.04	0.70
4	0.36	0.63	0.93	6.33	0.70
8	0.33	0.60	0.91	6.70	0.65
12	0.35	0.59	0.94	6.37	0.71

4.4. Effect of Ply Angles

The following subsection discusses how different ply angles contribute to the buckling load. We conducted analyses of critical buckling values under fully simply supported boundary conditions, using both analytical and numerical approaches for CNT volume fractions 0 and 8. The panel utilized in this study contains eight symmetrical plies for each angle, with consistent geometric and material properties as previously stated. As the angle approaches 90 degrees, the critical buckling force rises, as predicted. To elaborate, Table 4.5 provides the numerical and analytical results for CNT volume fraction 0, while Table 4.6 presents the analytical outcomes for CNT volume fraction values of 0 and 8. Figure 4.6 graphically illustrates the results.

Table 4.5. Analytical and Numerical (FEM) Results of Critical Buckling Load at Simply Supported Boundary Condition (SSSS) and Different Ply Angles with $V_{cnt} = 0\%$.

Lay-up	$N_{cr_{SSSS}}$ [N/mm] (Analytical)	$N_{cr_{SSSS}}$ [N/mm] (FEM)	Error (%)
0	8.05	8.03	0.29
15/-15	12.00	11.62	3.14
30/-30	21.92	20.57	6.15
45/-45	33.45	31.27	6.52
60/-60	42.65	40.69	4.60
75/-75	47.91	47.75	0.34
90	49.53	49.37	0.31

Table 4.6. Analytical Results of Critical Buckling Load at Simply Supported Boundary Condition (SSSS) and Different Ply Angles with 0% and 8% CNT Volume Fraction.

Lay-up	$N_{cr_{SSSS}}$ [N/mm] ($V_{cnt} = 0\%$)	$N_{cr_{SSSS}}$ [N/mm] ($V_{cnt} = 8\%$)	Difference (%)
0	8.05	9.26	14.99
15/-15	12.00	13.15	9.60
30/-30	21.92	22.95	4.69
45/-45	33.45	34.38	2.77
60/-60	42.65	43.56	2.12
75/-75	47.91	48.85	1.96
90	49.53	50.49	1.94

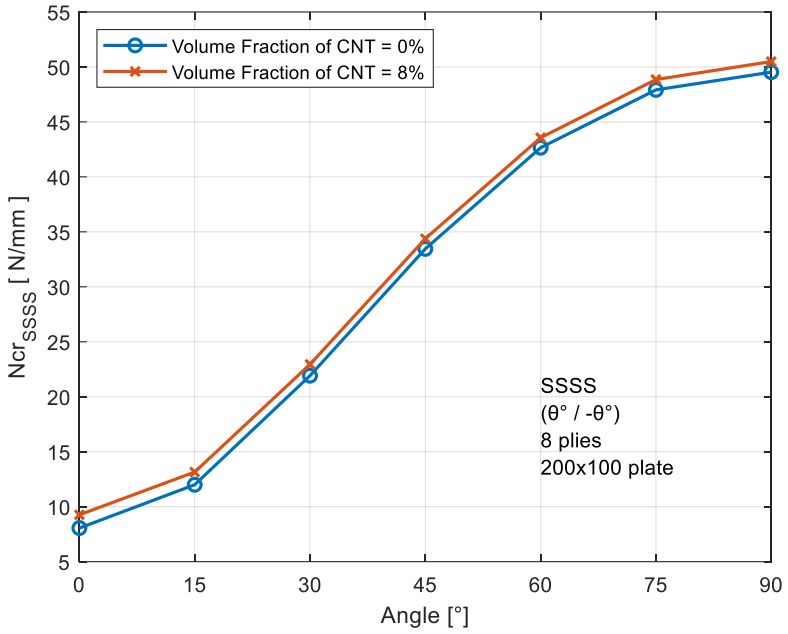

Figure 4.6. Graphical Representation of Analytical Results of Critical Buckling Load at Simply Supported Boundary Condition (SSSS) and Different Ply Angles with 0% and 8% CNT Volume Percentage.

The findings gathered show that utilizing CNTs dramatically boosts the laminate's critical buckling load. This increase can be particularly advantageous in composite applications. The findings were compared with those of studies in the literature, and similar outcomes were found. Figure 4.6 shows that the slope between 15 degrees and 75 degrees is steep, indicating a rapid increase in the critical buckling load at these angles. Moreover, when the lay-up is at 0 degrees, the percentage difference between CNT volume fractions 0 and 8 is higher, but this difference decreases as the angle approaches 90 degrees.

5. Buckling Load Of Different Types of Perforated Plates

The following chapter, the finite element method (FEM) is used to calculate buckling load that a rectangular composite panel with an elliptical cross-section can withstand under a uniaxial compression load. The elliptical hole is located in the center of the plate. Results were obtained by performing parametric studies that took into account the shape of the elliptical hole. These results were compared with the data obtained without a cutout. Figure 5.1 demonstrates that, as with the studies conducted in section 4, a 200x100 panel with 8 ply and a thickness of 1.016 mm was used in this study. The analysis was performed with constant ply angles. Parametric studies were conducted based on the c/d ratio and β angle, and the results of these studies were obtained.

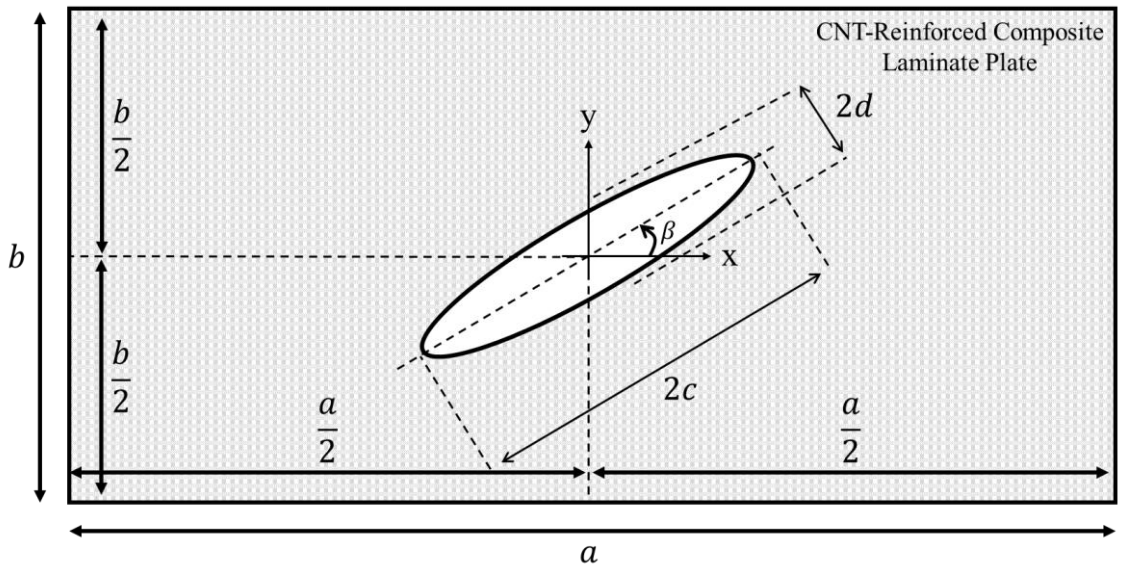

Figure 5.1. Geometry of the Model.

In the literature, researchers have undertaken several investigations on the buckling behavior of perforated composite plates. Komur et al. [33] performed parametric studies of a square-shaped composite plate by changing the geometric dimensions of the elliptic cutout and the stacking of the plate and obtained critical buckling loads using the finite element method (FEM). Rocha et al. [34] studied how to enhance the design of slender-hole, rectangular plates that are simply supported at all ends and prone to elastic buckling. The study took into account three distinct centered hole shapes: diamond, rectangular, and elliptical. A mathematical model was created using a finite element approach and the Lanczos method was employed. Abolghasemi et al. [35] investigate the buckle responses of isotropic plates having circular perforates under variable in-plane force. The buckling force is identified in two distinct stages: first by computing the pre-buckling stress distribution using a unique analytical methodology based on

coordinates with polarity and an endpoint integral, and then by using the Ritz method. This research investigates the effects of cut-out dimension, plate proportion of aspect, loaded distributions (constant, parabolic, and cosine), and various boundary constraints on buckling forces. As a result of the research of Abolghasemi et al. [35], it is observed that in the Simply Supported case and constant loading condition, if the ratio of the short side to the long side of the panel geometry is 0.5, which is, b/a = 0.5, the critical buckling load begins to increase after a certain cut-out diameter. This outcome can be depicted in Figure 5.2 by Abolghasemi et al. [35]. Mentioned in the Figure 5.2, D considered as the diameter of cut-out and L is the minimal value between a and b.

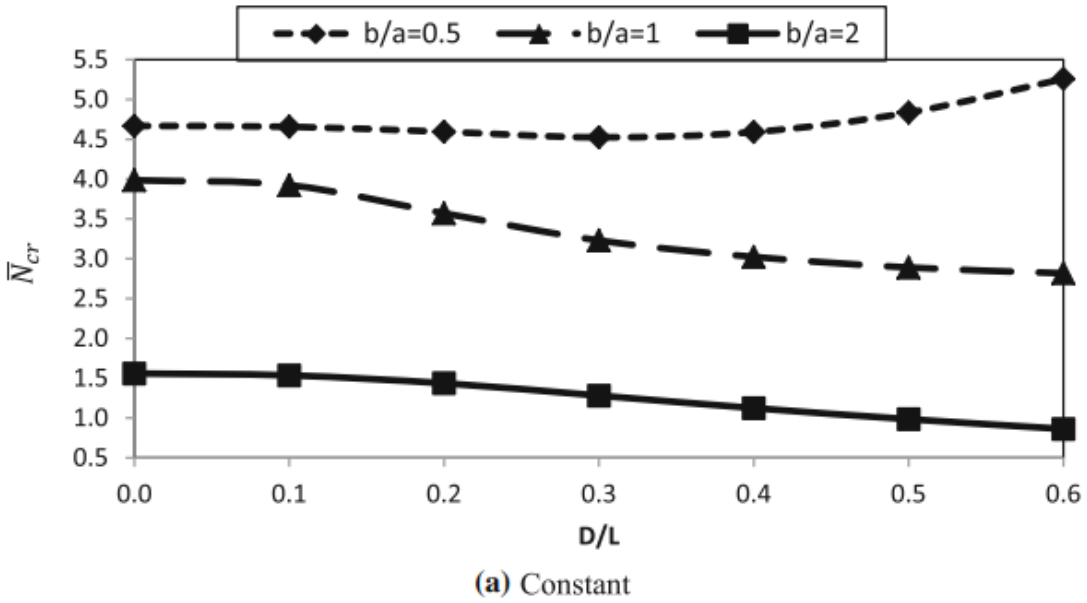

Figure 5.2. The impact of the width to height ratio on the buckling force of a plate with simply supported surrounds (SSSS) during uniaxial force. [35]

Srivastava et al. [36] utilize the technique of finite elements to investigate the loads of buckling in a longitudinal squared stiffened plate with a cross-sectional area of a square with distinct biaxial and uniaxial loadings applied at the plate edge. The forces are supposed to act on the flat mid-surface plane. The study uses the equation of motion to obtain characteristic formulae for natural frequencies, buckling forces, and mode shapes. Buckling force values for distinct modes underneath in-plane biaxial forces were calculated for a variety of edge situations. The computational investigation includes a hole-to-plate size range of 0, which varies from 0.8. The structural model addresses plates and stiffeners independently ensuring compatibility and flexible mesh division regardless of stiffener position. The research carried out demonstrates that when the cut-out diameter rises, the critical buckling load typically reduces, but in some circumstances gets higher.

5.1. Model Verification

The model was verified using a study carried out by Komur et al. [33], and the numerical findings acquired in this investigation were compared to the ones supplied by Komur et al. [33]. The outcomes demonstrate that the findings of the inquiry closely match the ones provided by Komur et al. [33] and this comparison can be shown in Figure 5.3. Consequently, the current work is believed applicable for the continuation of this study.

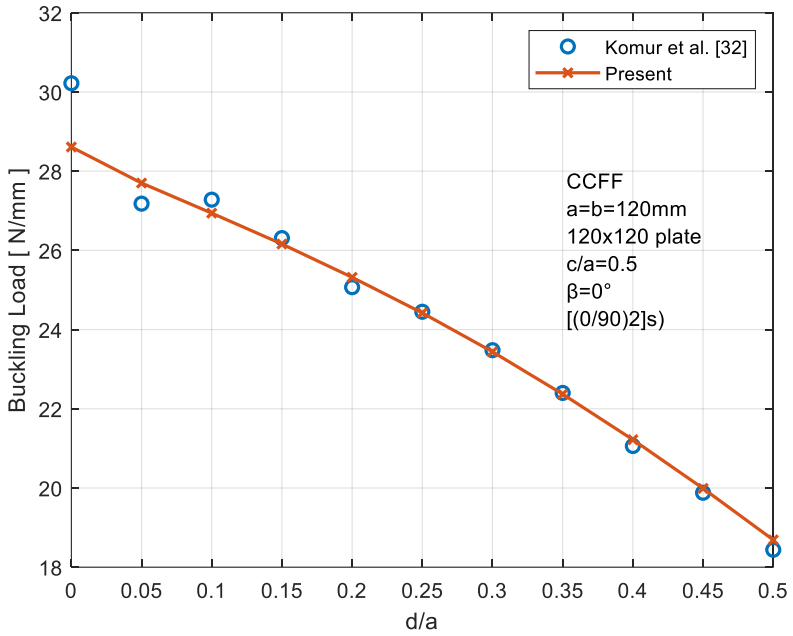

Figure 5.3. Comparison of maximum desired buckling load with Komur et al.'s findings [33].

5.2. c=d (Circular Hole)

When the c/d is equal to 1, the cutout geometry becomes a circular hole. Using different diameter values of this circular hole, critical buckling loads were obtained for CNT volume fractions 0 and 8. The panel was considered to have 8 plies arranged with 0-degree plies, that is, [0/0/0/0/0/0/0/0].

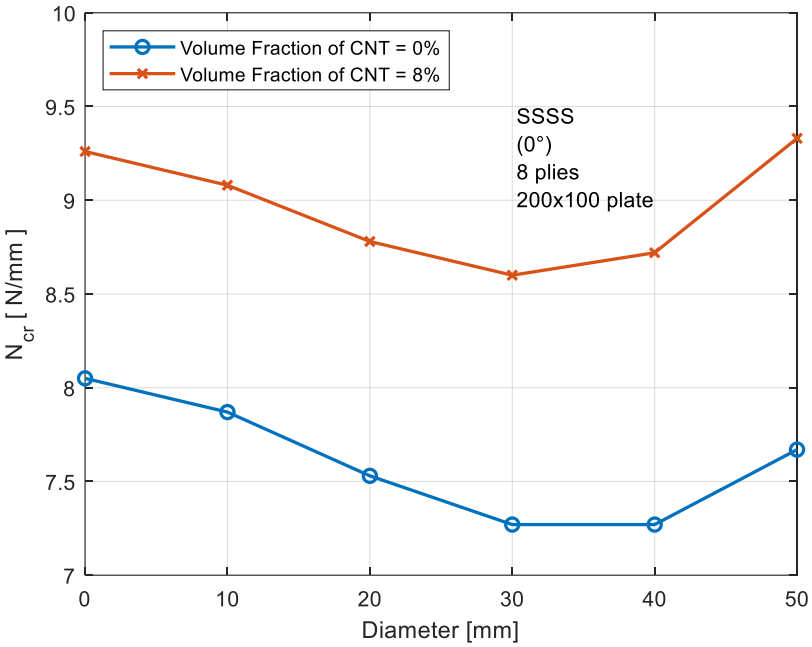

Figure 5.4. Effect of Diameter for Circular Hole (c=d).

Figure 5.4 illustrates how the critical buckling load reduces as the diameter rises. However, once it approaches a particular diameter, the threshold for buckling begins to rise again. This tendency was also seen in the study done by Abolghasemi et al. [35], as shared in Figure 5.2. As expected, increasing the volume fraction of CNT resulted in a considerable rise in the critical buckling load.

The impact of ply lay-up was thoroughly investigated on holes with diameters of 10 mm and 40 mm, and the obtained results were compared. A substantial difference was seen during the 0-degree ply stacking whereas the CNT volume percentage was 8, as opposed to the volume ratio of CNT of 0. However, in the case of 90-degree ply stacking, this difference was observed to decrease, emphasizing how the effects of ply lay-up can vary depending on hole diameters. The report contains the following facts: Table 5.1 and Figure 5.5 show the results for a 10 mm diameter, whereas Table 5.2 and Figure 5.7 reveal the results for a 40 mm diameter. The inquiry compares what comes out in-depth, noting the disparities.

Table 5.1. Effect of Stacking with 10 mm Hole Diameter.

Lay-up	$N_{cr_{SSSS}}$ [N/mm] ($V_{cnt} = 0\%$)	$N_{cr_{SSSS}}$ [N/mm] ($V_{cnt} = 8\%$)	Difference (%)
0	7.87	9.08	15.40
15/-15	11.48	12.66	10.28
30/-30	20.35	21.49	5.60
45/-45	30.74	31.86	3.64
60/-60	39.43	40.94	3.83
75/-75	45.67	46.68	2.21
90	47.95	49.02	2.23

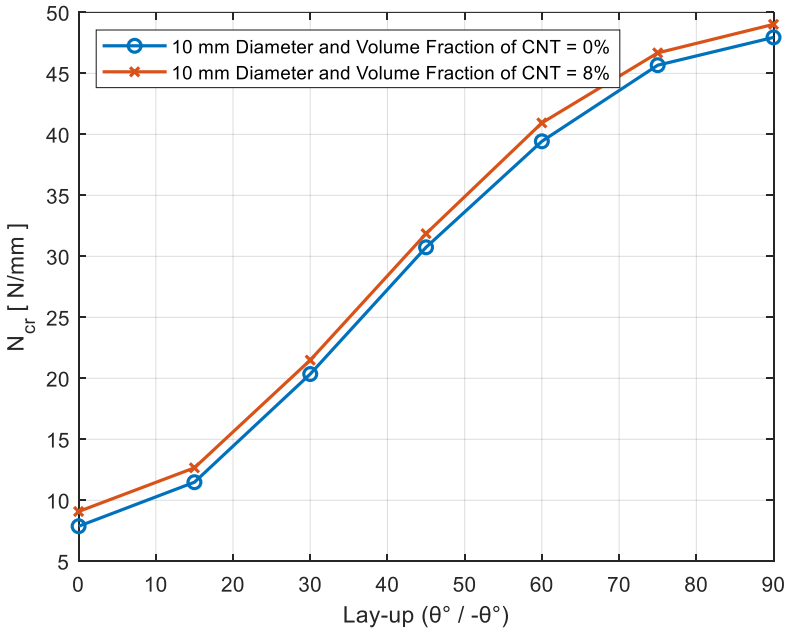

Figure 5.5. Effect of Stacking with 10 mm Hole Diameter.

The contour results of the plate with a hole diameter of 10 mm and a CNT volume fraction of 8% utilizing various stacking configurations are illustrated in Figure 5.6. The findings in Table 5.1 were obtained using these contours. Since there was a 100 mm edge on which the load was applied, the critical buckling value that resulted could be found by dividing by 100.

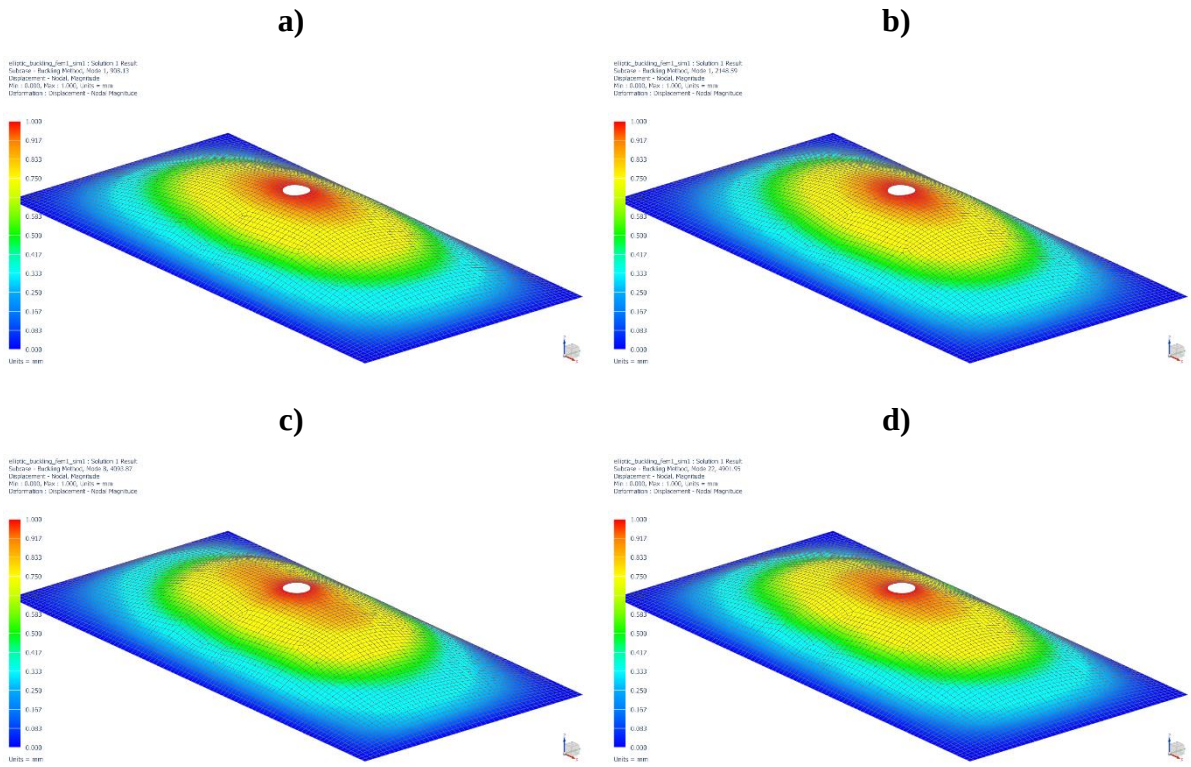

Figure 5.6. Buckled Model of 10 mm Hole Diameter Plate under Different Stacking with CNT Volume Fraction 8% (a) Lay-up 0°, (b) Lay-up 30°/-30°, (c) Lay-up 60°/-60° and (d) Lay-up 90°.

Table 5.2. Effect of Stacking with 40 mm Hole Diameter.

Lay-up	N_{crssss} [N/mm] ($V_{cnt} = 0\%$)	N_{crssss} [N/mm] ($V_{cnt} = 8\%$)	Difference (%)
0	7.27	8.72	19.94
15/-15	11.53	12.92	12.06
30/-30	20.84	22.26	6.81
45/-45	28.54	29.99	5.08
60/-60	49.00	52.25	6.63
75/-75	57.87	61.35	6.01
90	51.95	55.02	5.91

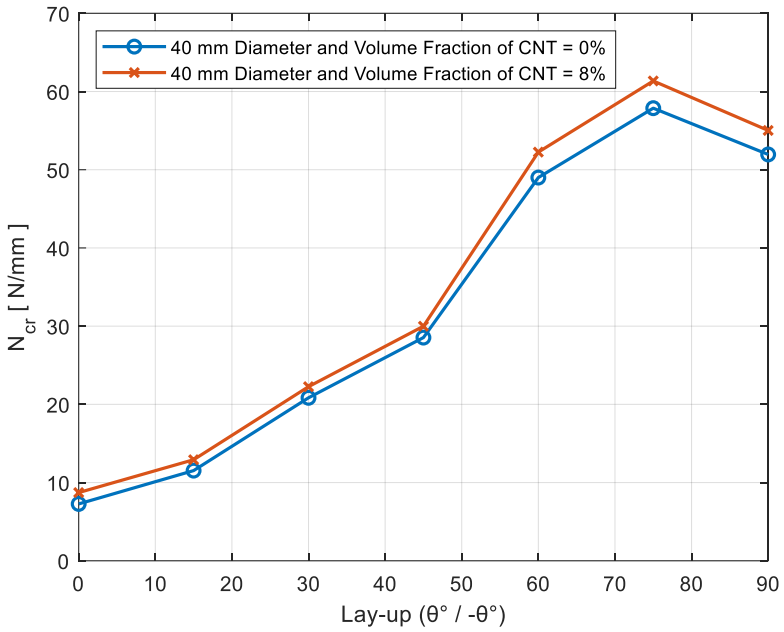

Figure 5.7. Effect of Stacking with 40 mm Hole Diameter.

In the study conducted on a 200x100 mm plate with 8 plies and a 20 mm hole diameter, the results were observed by changing the ply stacking and CNT volume fractions, and these changes are presented in detail in Table 5.3 and Figure 5.8. According to the data obtained, it was observed that the critical buckling value increased to its maximum level in the lay-up 90 configurations. Additionally, it was determined that this critical buckling value decreased when the CNT volume fraction was 8%. Parameters such as lay-up and CNT volume fraction appear to play a significant role in this study.

Table 5.3. Effect of CNT Volume Fraction with 20 mm Hole Diameter.

V_{cnt}	N_{crssss} [N/mm] (Lay-up 0°)	N_{crssss} [N/mm] (Lay-up 45°/-45°)	N_{crssss} [N/mm] (Lay-up 90°)
0	7.53	29.56	46.27
2	8.24	30.26	46.83
4	8.59	30.60	47.31
8	8.78	30.79	47.57
12	8.66	30.67	47.40

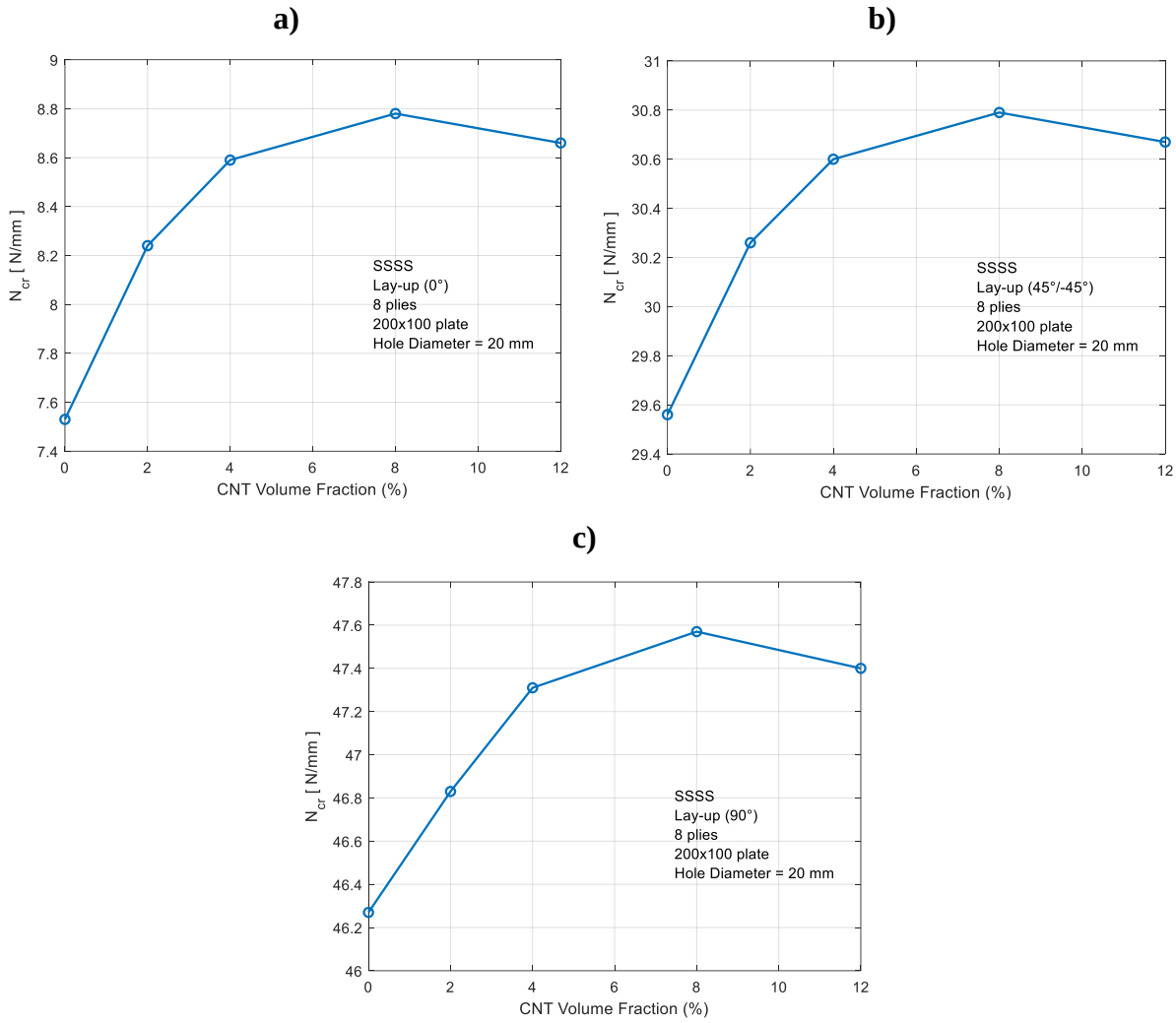

Figure 5.8. Effect of CNT Volume Fraction with 20 mm Hole Diameter (a) Lay-up 0°, (b) Lay-up 45°/-45° and (c) Lay-up 90°.

The waviness factor should also be taken into consideration when dispersing the carbon nanotube into the resin. If the amplitude (A) value shown in Figure 3.2 is high, the waviness factor decreases and has a negative effect on the material properties. The values seen in Table 5.4 were concluded and evaluated for a panel consisting of 8 plies at 0-degree lay-up and with a hole diameter of 20 mm. CNT volume fraction was taken as 8%. As can be seen from Figure 5.9, as the waviness factor increases, further, the threshold of buckling load rises. Consequently, the shorter the amplitude of the CNT, the more positively it affects the mechanical properties.

Table 5.4. Impact of Waviness Factor on Critical Buckling Load in a 0-degree, 8 Plies and 20mm Perforated Panel.

f_w	$N_{cr_{SSSS}}$ [N/mm]
0.2	7.87
0.3	8.12
0.4	8.36
0.5	8.58
0.6	8.78
0.7	8.97
0.8	9.16
0.9	9.33
1.0	9.49

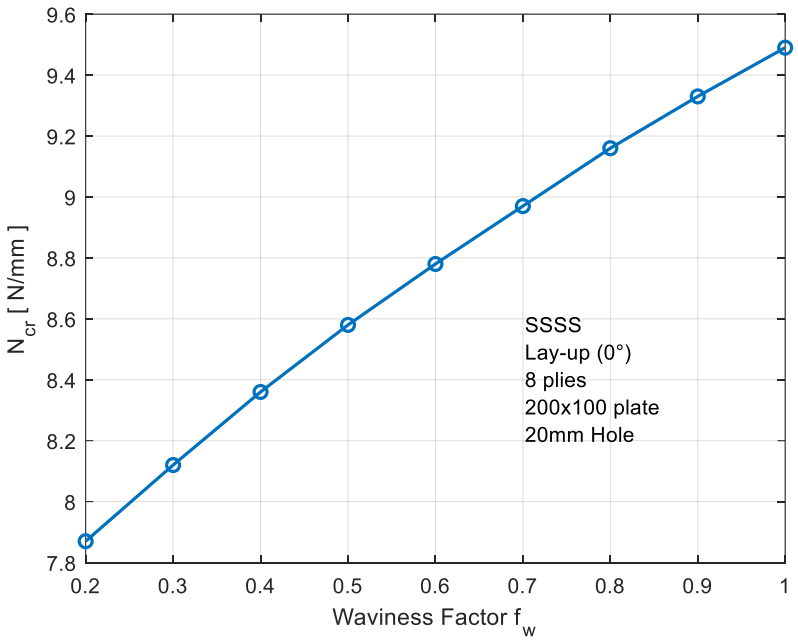

Figure 5.9. Graphical Representation of Effect of Waviness Factor on Critical Buckling Load in a 0-degree, 8 Plies and 20mm Perforated Panel.

5.3. c≠d (Elliptical Hole)

In cases where c/d ratio deviates from 1, the cut-out geometry turns into an elliptical hole. Different β angles and varied c/d ratios will be utilized in this study. The geometry of the panel with an elliptical hole and the applied configurations are depicted in Figure 5.10.

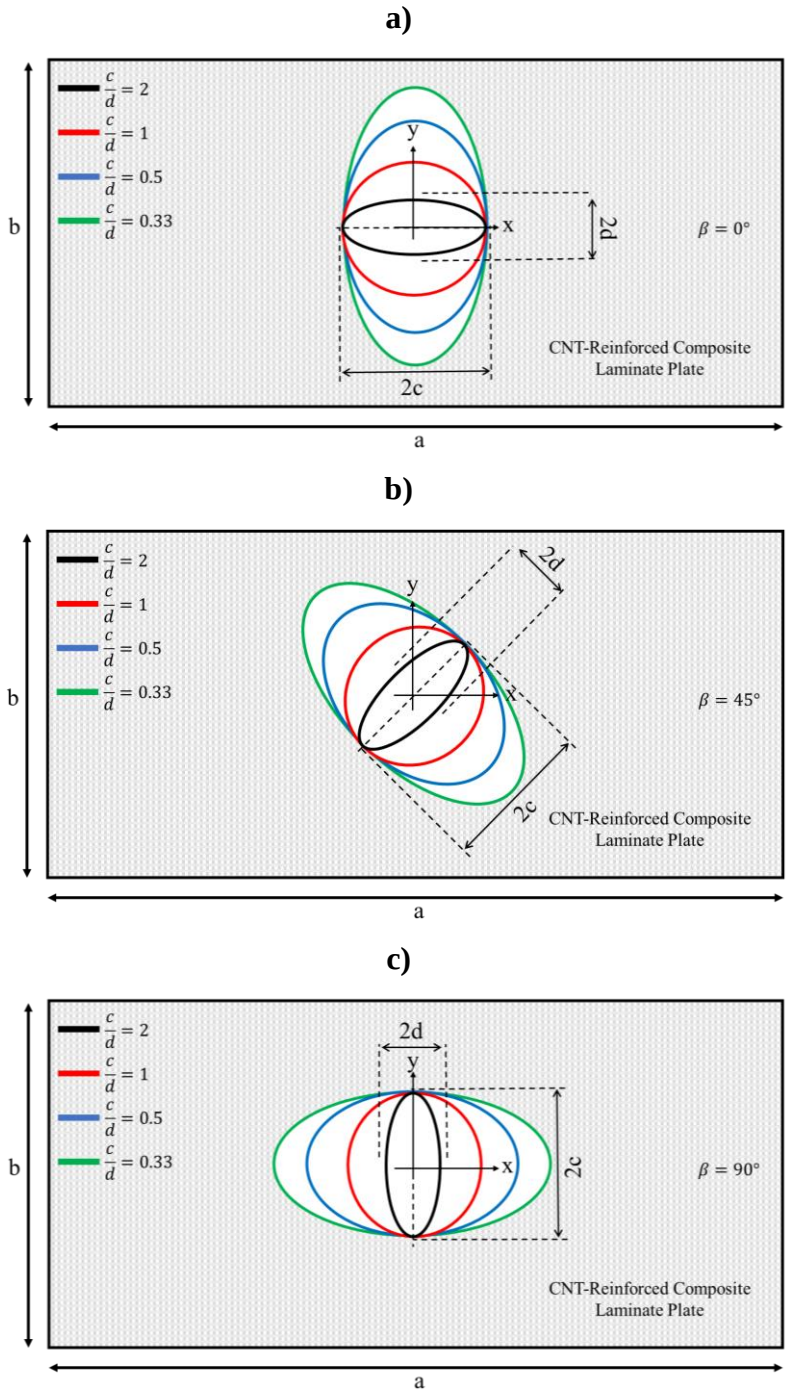

Figure 5.10. Geometry of the Panel with an Elliptical Hole (a) β=0°, (b) β=45° and (c) β=90°.

Critical buckling loads were evaluated for both CNT volume fractions: 0% and 8% for various radius ratios and different β angles for this elliptical hole. The structural configuration of the

panel was designed with 8 layers arranged in only 0-degree plies, defined as [0/0/0/0/0/0/0/0]. A thorough tabulation of the data is provided in Table 5.5, which presents the findings. Figure 5.11 also includes a graphical representation that provides a visual understanding of the observed data.

Table 5.5. Impact of c/d Variation on the Critical Buckling Load [N/mm] for CNT Volume Fractions of 0% and 8% with Different β Angles.

$\boldsymbol{\beta}$	$\boldsymbol{V_{cnt}}$ **(%)**	$\frac{c}{d} = 0.33$	$\frac{c}{d} = 0.50$	$\frac{c}{d} = 1.00$	$\frac{c}{d} = 2.00$
0°	0	11.77	8.22	7.53	7.64
	8	14.17	9.79	8.78	8.83
45°	0	8.01	7.44	7.53	7.74
	8	9.62	8.79	8.78	8.98
90°	0	6.19	6.85	7.53	7.86
	8	7.25	8.01	8.78	9.15

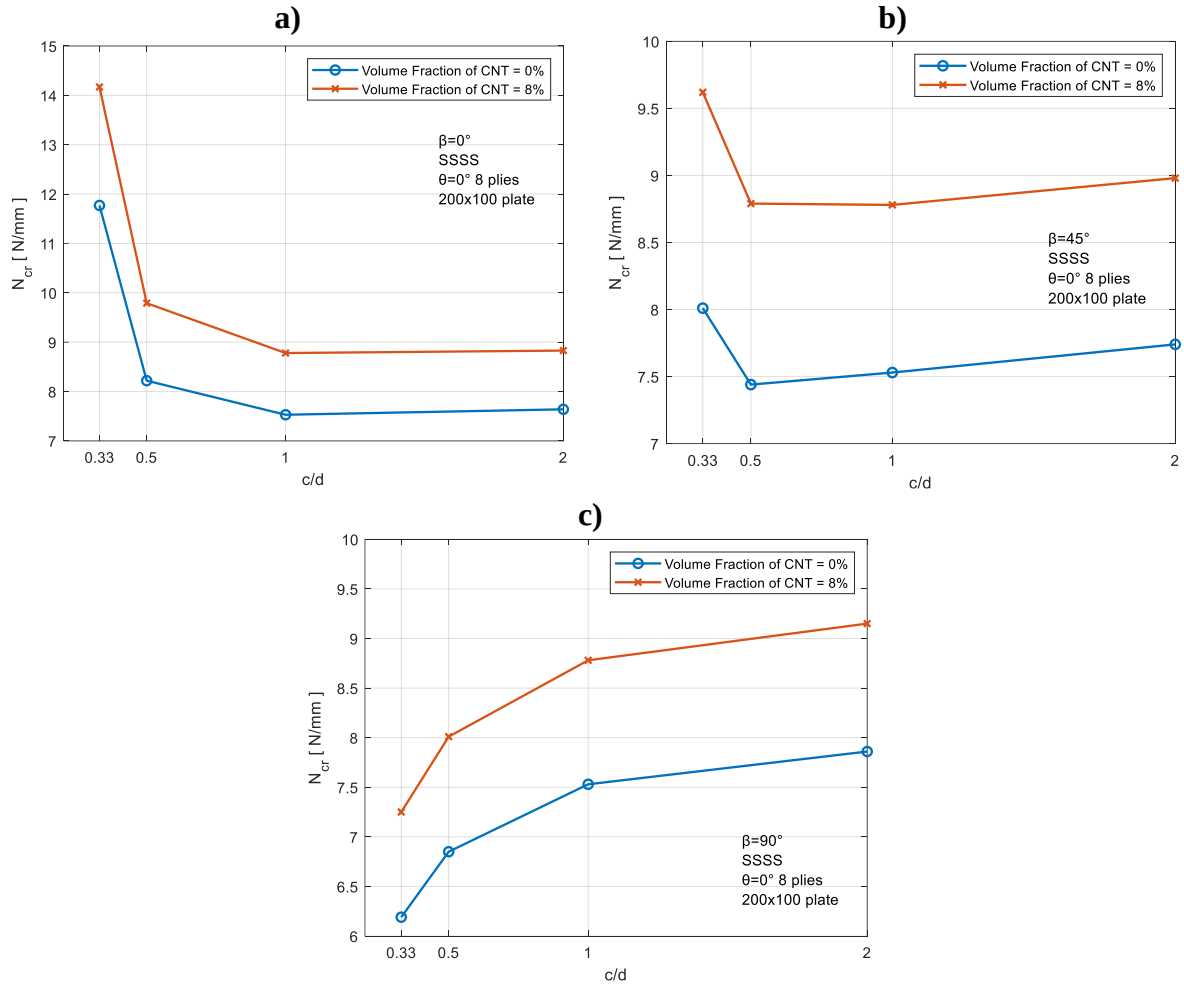

Figure 5.11. Effect of c/d Ratio for CNT Volume Fractions of 0% and 8% with Different β Angles (a) β=0°, (b) β=45° and (c) β=90°.

It is noteworthy that this investigation explores diverse mechanical responses associated with varying sizes of elliptical holes and sheds light on how geometry alters critical buckling loads in the context of CNT volume fractions.

In an elliptical configuration, that is, with an inclined hole (β=45°), the critical buckling load is less of a bearing on the major and minor radius ratios of the ellipse. This statement implies that the change in the dimensions of the ellipse has a comparatively smaller impact on the crucial buckling loads whereas the hole is in an inclined position. Put differently, as the shape of the ellipse changes in an inclined hole, these alterations have a more limited effect concerning the critical buckling force.

Figure 5.12 displays the contour outcomes for the plate with 0-degree stacking, β=45° and an 8% CNT volume fraction using different c/d ratios. These contours were used to generate the numerical values shown in Table 5.5. The load is applied on a 100 mm edge, so dividing the resultant critical buckling value by 100 yields the real value.

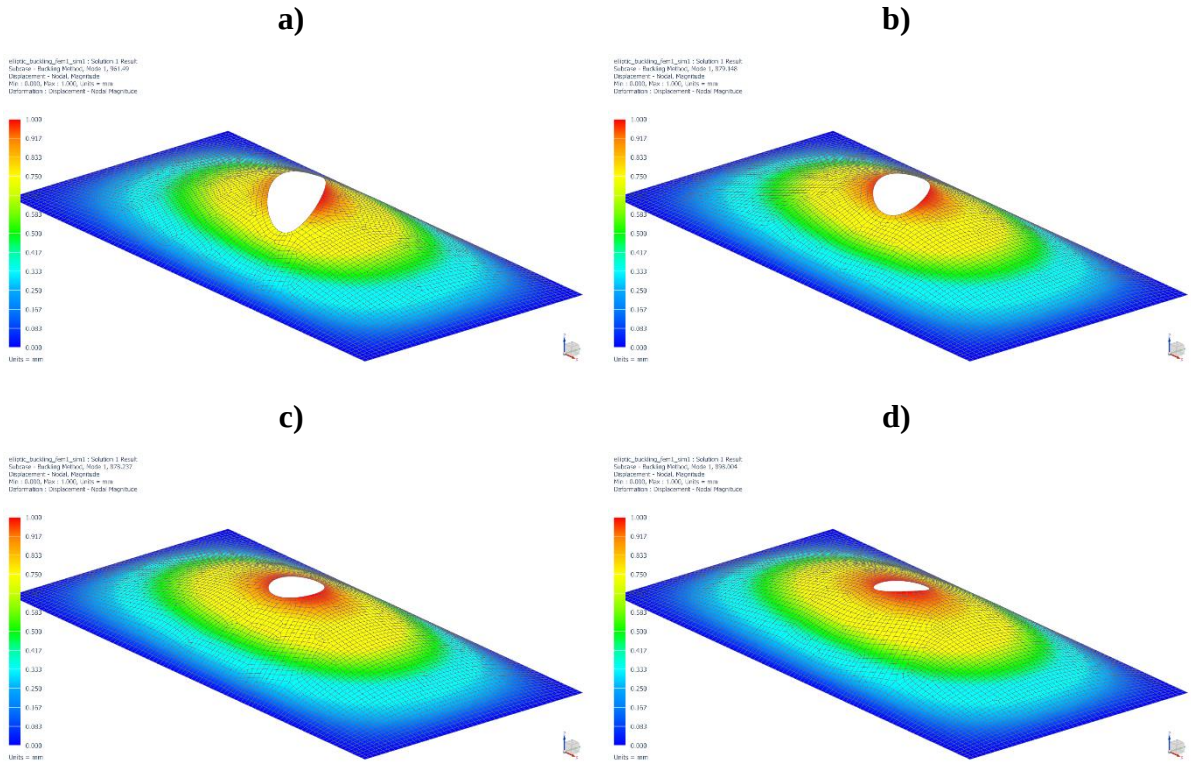

Figure 5.12. Buckled Model of Plate under Different c/d Ratios with β=45°, CNT Volume Fraction 8% and 0-Degree Lay-up (a) c/d=0.33, (b) c/d=0.50, (c) c/d=1.0 and (d) c/d=2.0.

The impact of ply alignments with various c/d ratios regarding critical buckling load was examined when the ellipse had been positioned at 45 degrees (β=45°). The results obtained are presented in detail in Table 5.6, as well as their graphical representation in Figure 5.13. As can be clearly seen from Table 5.6, it was observed that the CNT effect decreased in percentage when the ply angles were 90 degrees. In other words, when the ply angles are 0 degrees, the CNT effect becomes more noticeable.

As can be seen from Figure 5.13, When the ply angles were shifted from 15 degrees to 75 degrees, the critical buckling force surged dramatically. This shows that changes in ply angles within a certain range had an enormous impact in terms of critical buckling force.

The critical buckling load seemed to diminish as the c/d ratio fell and the ply angles approached 90 degrees. These findings highlight the need of thoroughly examine the bearing of c/d fraction as well as ply angles on the threshold of buckling load. These characteristics play a vital role in establishing the mechanical features of the material.

Table 5.7 shows how the ply thickness of a 0-degree 8 plies laminate affects the critical buckling load. While gathering these results, the beta angle was fixed at 45-degree. As expected, the buckling force rises with thickness. The c value remained constant while the d value was increased. As the d value increased, correspondingly increased the difference between CNT Volume Fractions 0% and 8%.

Table 5.6. Impact of Laminate Lay-up on Critical Buckling Load [N/mm] for 0% and 8% CNT Volume Fractions with Different c/d Ratios and β=45°.

	c=10 mm d=5 mm			c=d=10 mm			c=10 mm d=15 mm			c=10 mm d=20 mm		
Lay-up	**Vcnt=0%**	**Vcnt=8%**	**Difference (%)**	**Vcnt=0%**	**Vcnt=8%**	**Difference (%)**	**Vcnt=0%**	**Vcnt=8%**	**Difference (%)**	**Vcnt=0%**	**Vcnt=8%**	**Difference (%)**
0	7.74	8.98	16.02	7.53	8.78	16.60	7.42	8.71	17.39	7.44	8.79	18.15
15/-15	11.39	12.58	10.45	11.23	12.44	10.77	11.24	12.47	10.94	11.44	12.74	11.36
30/-30	20.17	21.33	5.75	19.94	21.12	5.92	20.01	21.23	6.10	20.48	21.78	6.35
45/-45	30.07	31.26	3.96	29.56	30.79	4.16	29.28	30.57	4.41	29.24	30.61	4.69
60/-60	38.25	40.10	4.84	38.04	40.36	6.10	38.21	40.96	7.20	45.30	48.48	7.02
75/-75	40.73	44.39	8.99	45.21	46.01	1.77	46.82	48.60	3.80	48.90	52.35	7.06
90	46.94	48.46	3.14	46.27	47.57	2.81	46.07	47.80	3.62	47.14	48.76	3.32

Table 5.7. Impact of Ply Thickness on Critical Buckling Load [N/mm] for 0% and 8% CNT Volume Fractions with Different c/d Ratios, 8 plies 0-Degree Laminate and β=45°.

	c=10 mm d=5 mm			c=d=10 mm			c=10 mm d=15 mm			c=10 mm d=20 mm		
t [mm]	**Vcnt=0%**	**Vcnt=8%**	**Difference (%)**	**Vcnt=0%**	**Vcnt=8%**	**Difference (%)**	**Vcnt=0%**	**Vcnt=8%**	**Difference (%)**	**Vcnt=0%**	**Vcnt=8%**	**Difference (%)**
0.1	3.79	4.39	15.83	3.68	4.29	16.58	3.63	4.28	17.91	3.64	4.30	18.13
0.2	30.12	34.93	15.97	29.30	34.17	16.62	28.86	33.87	17.36	28.90	34.17	18.24
0.3	100.98	117.12	15.98	98.28	114.61	16.62	96.74	113.55	17.38	96.78	114.45	18.26
0.4	237.61	275.66	16.01	231.36	269.83	16.63	227.59	267.21	17.41	227.48	269.10	18.30

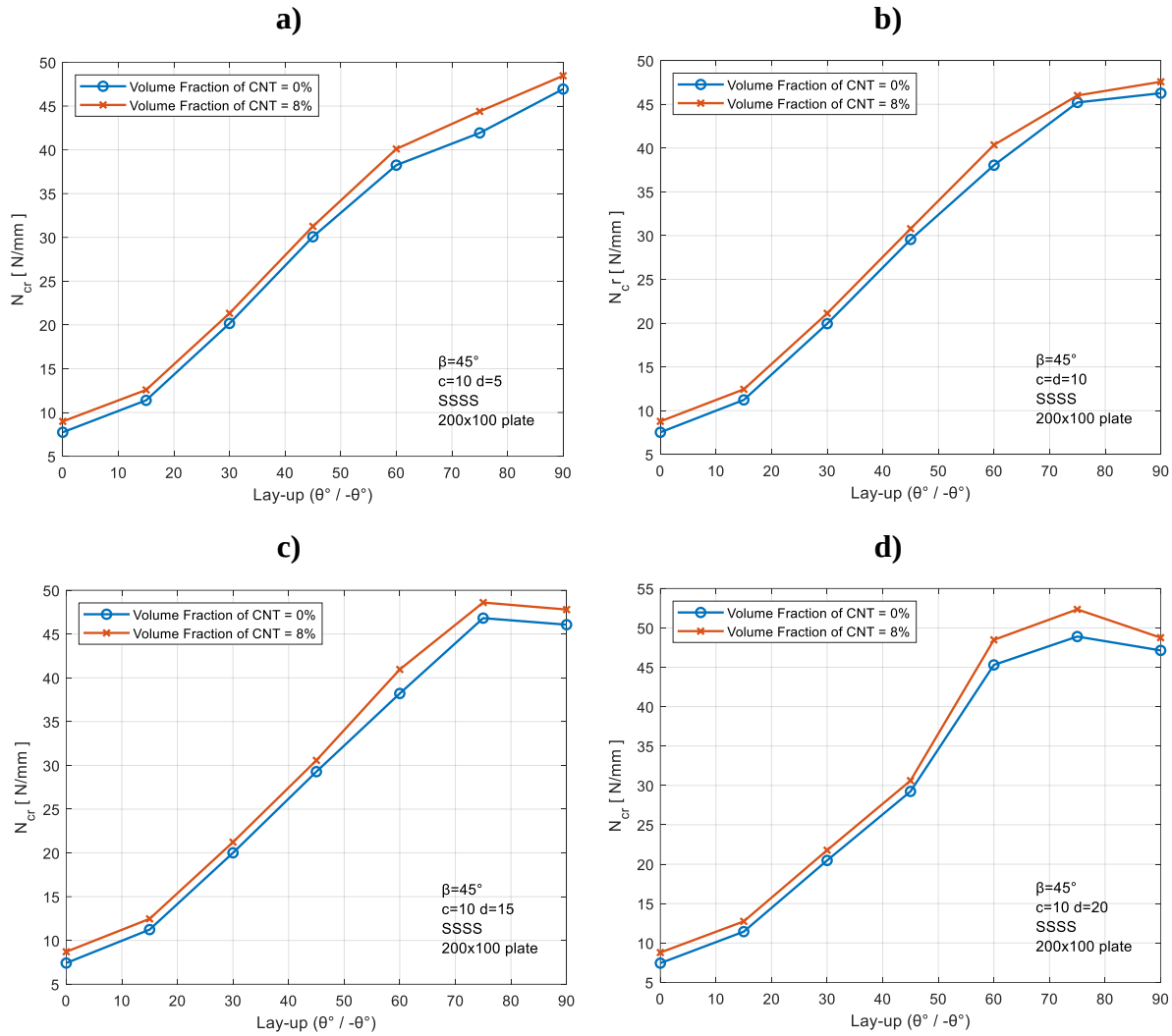

Figure 5.13. Impact of Laminate Lay-up on Critical Buckling Load for 0% and 8% CNT Volume Fractions with Different c/d Ratios (a) c/d=2, (b) c/d=1, (c) c/d=0.66 and (d) c/d=0.5.

The contour findings utilizing various beta values (ß=0, 45, and 90) for a plate with an elliptical hole, 0-degree ply stacking, an 8% CNT volume fraction, c=10 mm, and d=5 mm are displayed in Figure 5.14. Table 5.5 displays the numerical values that were generated using these contours. The actual value can be obtained by dividing the critical buckling value that results from applying the load to a 100 mm edge by 100.

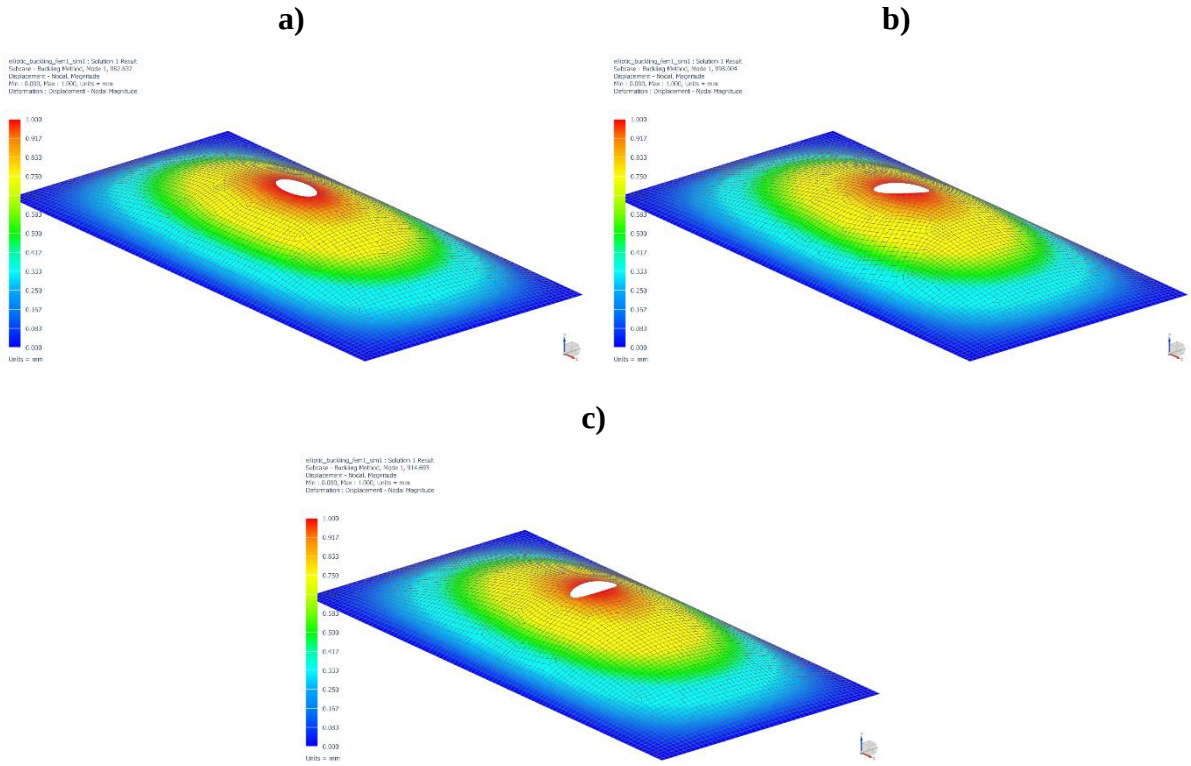

Figure 5.14. Buckled Model of Plate under Different β Angles with c=10 mm and d=5 mm, CNT Volume Fraction 8% and 0-Degree Lay-up (a) β=0°, (b) β=45°, and (c) β=90°.

Figure 5.15 illustrates the contour results for a plate with an elliptical hole at a 45-degree angle to the x-axis, an 8% CNT volume fraction, and dimensions of c=10 mm and d=5 mm, using various ply stackings. These contours were utilized to generate the numerical values displayed in Table 5.6. Since the load is applied to a 100 mm edge, dividing the calculated critical buckling value by 100 yields the actual value.

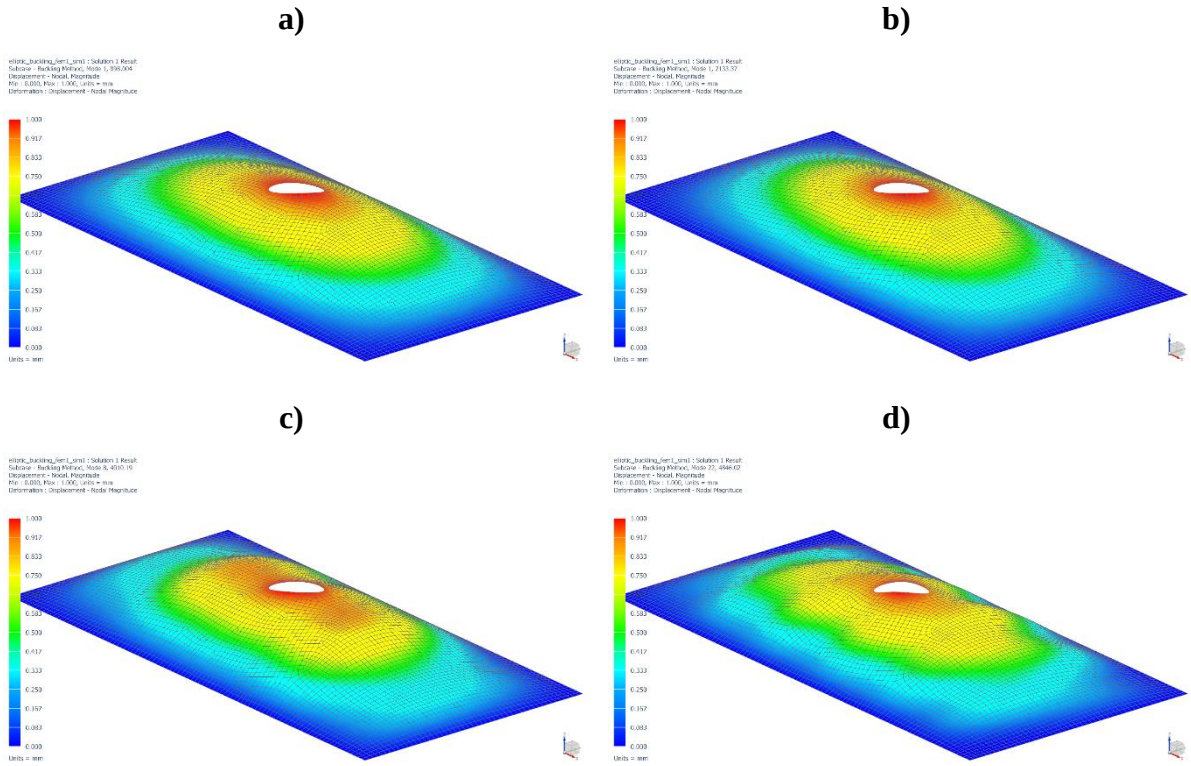

Figure 5.15. Buckled Model of Plate under Different Ply Stackings with β=45°, CNT Volume Fraction 8% and c/d=2 (a) Lay-up 0°, (b) Lay-up 30°/-30°, (c) Lay-up 60°/-60° and (d) Lay-up 90°.

Figure 5.16 depicts contour findings utilizing various ply thickness values (0.1, 0.2, 0.3, and 0.4 mm) for a plate with elliptical holes, 0-degree 8 plies stacking, 8% CNT volume fraction, c = 10 mm, and d = 5 mm. Table 5.7 displays the numerical values calculated using these contours. The actual value can be calculated by dividing the critical buckling value obtained from applying the load to a 100 mm edge by 100.

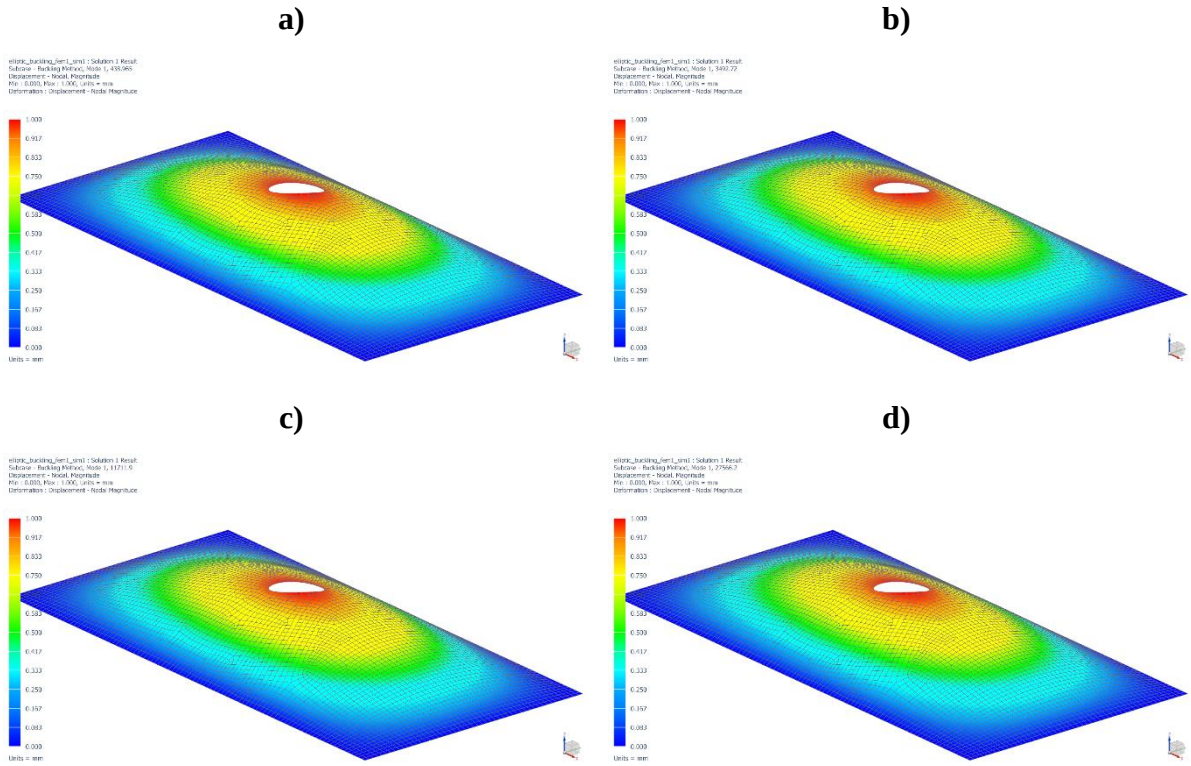

Figure 5.16. Buckled Model of Plate under Different Ply Thickness with β=45°, CNT Volume Fraction 8%, 0-Degree 8 Plies, c = 10 mm, d = 5 mm (a) 0.1 mm (b) 0.2 mm, (c) 0.3 mm and (d) 0.4 mm.

In the study conducted on an 8-plies plate with dimensions of 200x100 mm, the c/d ratio was set at 0.66, and the orientation angle of the ellipse was fixed at 45 degrees. Various studies were performed by altering the CNT volume fractions, and the results, along with detailed information on these variations, are presented in Table 5.8 and Figure 5.17.

Table 5.8. Effect of CNT Volume Fraction when c/d=0.66 and β=45°.

V_{cnt}	$N_{cr_{SSSS}}$ [N/mm] (Lay-up 0°)	$N_{cr_{SSSS}}$ [N/mm] (Lay-up 45°/-45°)	$N_{cr_{SSSS}}$ [N/mm] (Lay-up 90°)
0	7.42	29.28	46.07
2	8.15	30.01	47.05
4	8.51	30.37	47.53
8	8.71	30.57	47.80
12	8.58	30.44	47.63

a)

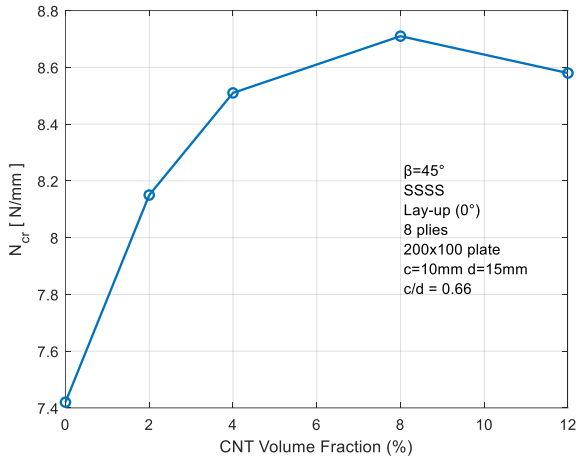

b)

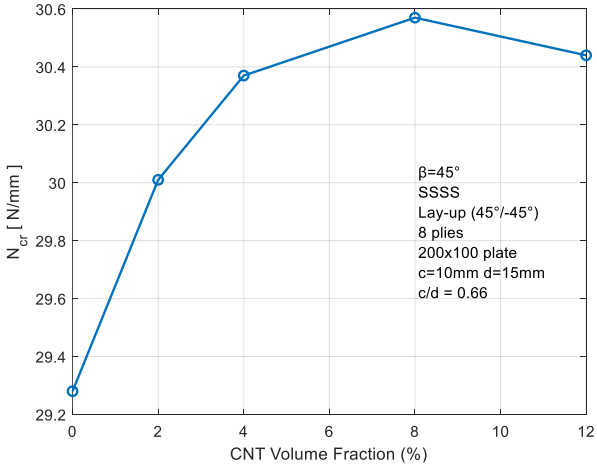

c)

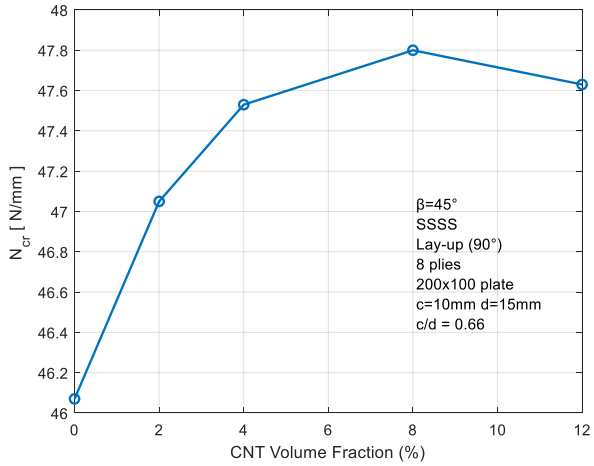

Figure 5.17. Impact of CNT Volume Percentage when c/d=0.66 and β=45° **(a)** Lay-up 0°, **(b)** Lay-up 45°/-45° and **(c)** Lay-up 90°.

According to the obtained data, when the c/d ratio of the plate was set at 0.66, the critical buckling value reached its maximum level in the 90-degree stacking configuration. This indicates that, under a specific combination of hole diameter and number of plies, the highest critical buckling value was achieved in the 90-degree lay-up configuration.

The largest critical buckling value could be detected when the CNT volume percentage was 8%. After reaching this proportion, the critical buckling force of the plate began to fall, demonstrating that factors such as lay-up and CNT volume fraction, particularly in specific geometric configurations, had an important bearing on the plate's critical buckling load.

An investigation was conducted on the critical buckling load's sensitivity to the waviness factor when the c/d ratio deviates from 1.0. As previously mentioned, if the amplitude value in Figure 3.2 is high, the waviness factor reduces and adversely affects the qualities of the material when the c/d ratio equals 1. The values seen in Table 5.9 were concluded and evaluated for the c/d ratio of 0.5, the β angle (the angle of the ellipse to the x-axis) of 45 degrees, and for the panel where the plies were draping at 0 degrees and formed an 8-ply laminate. An 8% volume fraction of CNT was utilized. Figure 5.18 illustrates how the critical buckling load rises with increasing waviness factor. Consequently, the mechanical properties are more positively impacted by CNTs with shorter amplitude.

Table 5.9. Effect of Waviness Factor on Critical Buckling Load in a 0-degree, 8 Plies Perforated Panel when c/d=0.5 and β=45°.

f_w	$N_{cr_{ssss}}$ [N/mm]
0.2	7.80
0.3	8.08
0.4	8.33
0.5	8.57
0.6	8.78
0.7	9.00
0.8	9.20
0.9	9.38
1.0	9.56

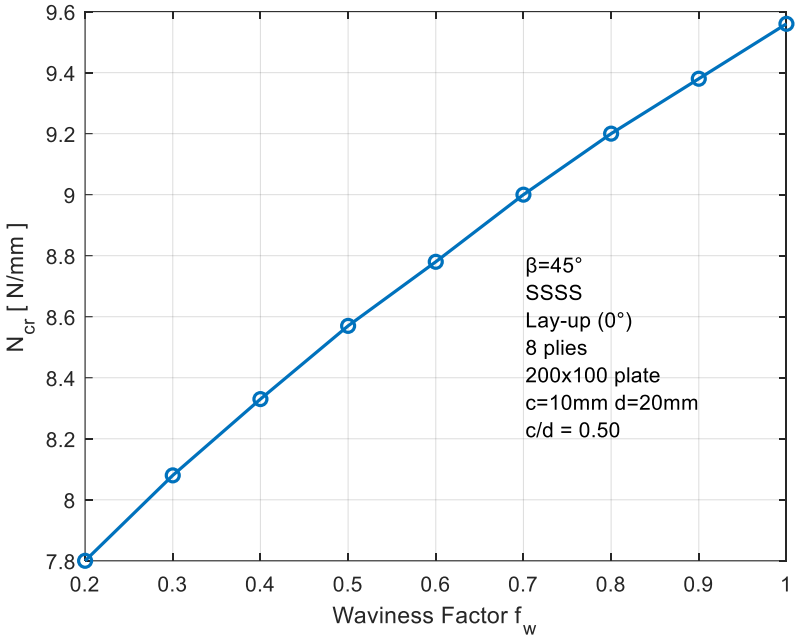

Figure 5.18. Graphical Representation of Effect of Waviness Factor on Critical Buckling Load in a 0-degree, 8 Plies Perforated Panel when c/d=0.5 and β=45°.

6. Conclusion and Future Work

6.1. Conclusions

To strengthen composite materials generally used in aircraft, carbon nanotubes (CNT) can be dispersed into composite resin to produce composite laminates with better structural and material properties. The fundamental goal of the investigation is to understand the buckling capabilities of composite plates reinforced with CNT and determine the critical buckling load. The study initially generated analytical equations to predict the buckling load, followed by numerical simulations using Finite Element Analysis (FEA). This comprehensive approach enabled a detailed examination of the behavior of the plate under various conditions.

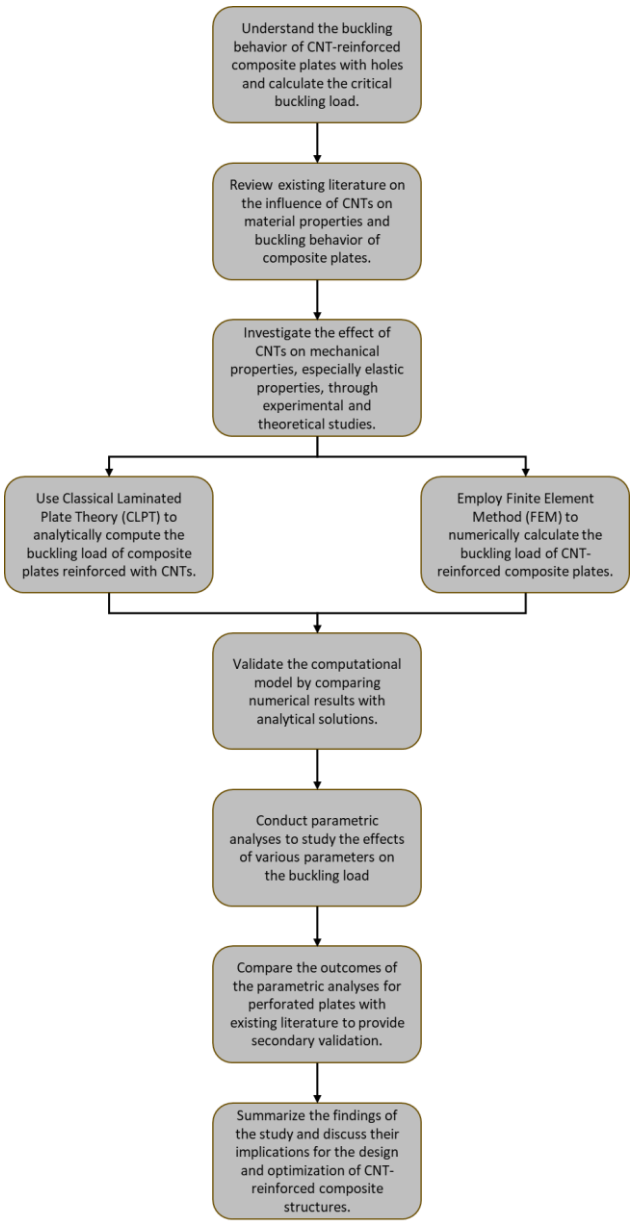

Figure 6.1. The General Procedure Developed for the Present Study

The development of CNT, manufacturing methods, and research into composite plate buckling analysis were all investigated. The study focuses on the buckle and buckling properties of nanocomposite plates, with a special emphasis on their behavior when perforated. The ultimate goal of this research is to grasp the buckling characteristics of composite plates reinforced by carbon nanotubes. Furthermore, this investigation intends to determine the threshold load for buckling of various types of holes.

The equations provided by Classical Laminated Plate Theory (CLPT), which emerged from the Kirchhoff's hypothesis, were used to determine the stiffness matrix of thin plates. The critical buckling load calculations were calculated using the formulae published by A. W. Leissa [1]. The formula that governs was determined using an orthotropic and homogeneous plate. This formula was then used to compute the critical load that causes buckling for different constraints on the boundary. Analytical findings were obtained by applying the threshold load for buckling formulae.

The material characteristics of a CNT-reinforced composite plate were calculated using the Rule of Mixtures and Halpin-Tsai techniques. These approaches are frequently used to estimate the structural features of a material. The Rule of Mixtures makes predictions derived from the proportions that correspond to the material's various components. Halpin-Tsai, on the other hand, makes more specific predictions through the use of factors such as component proportions, structural characteristics, and interactions with one another. Halpin-Tsai provides more sensitive and accurate results than the Rule of Mixtures. The fiber and resin ratios were taken as 60% and 40%, respectively, and the mechanical properties of the material were found using these methods.

Based on the mixing equations, it was observed that the waviness factor and agglomeration have an effect on the elastic characteristics of the CNT-reinforced laminate. The consequences might be summarized as follows:

- When the waviness factor approaches 1.0, which means the wavelength is zero, the elastic modulus increases. However, after a certain CNT volume section, the elastic modulus begins to decrease.
- As the agglomeration factor approaches 1.0, the elastic modulus increases linearly. On the other hand, as the agglomeration factor decreases, the elastic modulus decreases. Therefore, it is essential to homogeneously distribute CNT into the resin.

- An increase in the properties of the material with more volume proportion of CNT reduces the elastic and shear modulus, and there is a certain point where the amounts begin to decrease. This decrease is seen after the volume proportion of CNT is 8%, and values in the D matrix decrease significantly.

Consequently, the CNT volume fraction should be adjusted appropriately because an excessive increase in the ratio may adversely affect the material properties and correspondingly buckling loads.

The QUAD4 element from the Nastran library was used to construct the model for the finite element technique studies. A fully simply supported case (SSSS) was used as the boundary condition. The mesh convergence study provided the best finite element mesh configuration, balancing accuracy, and computational efficiency considerations. Since there was a difference of almost 0.125% between the mesh sizes of 2 mm and 1 mm, the analysis was continued by choosing a mesh size of 2 mm.

The following inferences can be made from the results obtained for the plate without holes:

Effect of CNT Volume Fraction,

- As mentioned about material properties, while the critical buckling load increases between CNT volume fractions 0% and 8%, a trend change and decrease was observed after 8%. This result was observed both analytically and with the finite element method (FEM).
- Error-values between FEM and analytical solutions were mostly observed in fully clamped boundary condition (CCCC). These inconsistencies arise from the presence of bending-flexion coupling terms within the stiffness matrix. In this case, FEM provides more realistic results compared to analytical approaches. This advantage arises from the fact that the analytical formulas used often cannot fully reflect the complex behavior of the system. On the other hand, FEM represents physical phenomena more accurately by introducing and comprehensively solving these coupling terms.

Effect of Ply Angles,

- Critical buckling load values for laminates with CNT volume fractions of 0% and 8% were determined using both analytical and numerical approaches. The data demonstrate how integrating CNTs into the laminate greatly raises the threshold of buckling force.
- It has been observed that the error value is high at angles between 0 and 90 degrees.

- It has been observed that when stacking is at 0 degrees, the difference between CNT volumes 0% and 8% is the most significant, and this difference decreases as the angle approaches 90 degrees.

The following inferences can be made from the results obtained for the perforated plate:

c=d (Circular Hole),

- The buckling load falls with diameter however, it raises over a particular diameter. This increase was reported by Abolghasemi et al. [35]. When the size of the plate gets bigger, there might be other issues to consider.
- The ply lay-up effect in holes with diameters of 10 mm and 40 mm was examined and the results were compared. Ply lay-up has a considerable influence in the case of 0-degree ply stacking, especially when the CNT volume percentage is 8%. However, it has been found that this effect decreases in the case of 90-degree ply stacking.
- The threshold for buckling force reduced as the hole diameter got higher, but increased above a particular diameter. As the hole diameter increases, the percentage difference between the 0% volume fraction and the 8% volume fraction also increases. These findings reveal that ply stacking and hole size need to be considered while designing composite structures.
- Critical loads for buckling were found by setting the hole diameter to 20 mm and varying the lay-up and volume percentage of CNT. Changing the stacking and CNT volume ratios on the plate has been shown to change the critical load for buckling. Whereas upper bound on the loads for buckling were observed in the 90-degrees stacking configuration, the minimum critical buckling loads were obtained in 0-degrees ply lay-up. Moreover, critical buckling loads decreased when the volume percentage of CNTs exceeded 8%.
- The waviness factor's impact on the critical buckling load was examined when the hole diameter was 20 mm. As mentioned before, the closer the waviness factor is to 1.0, the greater the critical buckling load. In other words, if the CNT has a low amplitude (A) value, the critical buckling load increases.

c≠d (Elliptical Hole),

- It has been observed that in an elliptical configuration with an angled hole (β=45°), Variations in the ellipse's minor and major radius ratios are less pronounced to the load for the buckling. This suggests that there is a limited contribution to the critical buckling load when adjusting the ellipse's size in the hole's inclined position.
- Examined were the impacts of various c/d percentages and ply angles on the material's critical buckling load. It has been observed that the CNT effect decreases when the Ply angles are 90 degrees but increases when it is 0 degrees. Additionally, it has been determined that ply angles varying within a certain range significantly affect the critical load for buckling. Once the c/d proportion decreased and the layer angles approached 90 degrees, there was a noticeable drop in the critical buckling load. These findings highlight the importance of the c/d ratio and layer angles in determining the mechanical resistance of the material against buckling.
- When the c/d ratio was fixed as 0.66 and the angle of the ellipse was fixed at 45 degrees, critical buckling loads were obtained at different CNT volume fractions and different lay-ups. The critical buckling load reached its maximum level at 90 degrees stacking. Additionally, as observed before, it was observed that when the volume percengate of CNT was 8%, the critical load for buckling was at its maximum level and started to decrease after this level. These outcomes demonstrate how the plate has a major impact on the threshold buckling load, especially in certain geometric configurations, and this effect can be related to parameters such as stacking and CNT volume fraction.
- At 0-degree lay-up, the impact of various waviness factors on the critical load that causes buckling was examined when the CNT volume fraction was 8%, the c/d ratio was 0.5 and the angle of the ellipse was 45 degrees. It had been demonstrated that when the CNT's amplitude arose, the load required for buckling dropped. In other words, as the waviness factor approaches 1.0, the material's mechanical characteristics are improved and hence exhibit greater buckling load.

6.2. Future Works

Possible future research endeavors could be outlined as follows.

- Research attempts might be focused on understanding the consequences of biaxial loading.
- Structural integrity may be improved by looking at the best locations and number of holes.
- Research on various loading profiles, such as sinusoidal, parabolic, and so on, can provide information on various load distributions.
- Critical buckling thresholds impacted by transverse loading circumstances can be clarified by analyzing the buckling behavior of plates, especially those subjected to a 90-degree surface pressure load.
- The buckling performance of curved panels with carbon nanotube reinforcement and perforations may be investigated further in order to improve design considerations and our comprehension of intricate structural reactions.

REFERENCES

[1] Haim Abramovich (2017). Stability and Vibrations of Thin-Walled Composite Structures. Woodhead Publishing.

[2] Vidu, Ruxandra & Rahman, Masoud & Mahmoudi, Morteza & Enachescu, Marius & Poteca, Teodor & Opris, Ioan. (2014). Nanostructures: A Platform for Brain Repair and Augmentation. Frontiers in systems neuroscience. 8. 91. 10.3389/fnsys.2014.00091.

[3] Iijima, S. (1991). Helical microtubules of graphitic carbon. *nature*, 354(6348), 56-58.

[4] Muhammad Usama Arshad, Congjie Wei, Yanxiao Li, Jiaoli Li, Moein Khakzad, Chuanrui Guo, Chenglin Wu, Mohammad Naraghi, Mechanics – Microstructure relations in 1D, 2D and mixed dimensional carbon nanomaterials. Carbon 204 (2023) 162-190, https://doi.org/10.1016/j.carbon.2022.12.042

[5] Dindar, B., "Experimental investigation of the effect of nanoparticular additives on fatigue, buckling and impact behaviour of fiber reinforced composites" Doctoral Thesis, Pamukkale University Institute of Science, Department of Mechanical Engineering, Denizli, 2019

[6] Soni, Sourabh & Thomas, Benedict & Kar, Vishesh. (2020). A Comprehensive Review on CNTs and CNT-Reinforced Composites: Syntheses, Characteristics and Applications. Materials Today Communications. 25. 101546. 10.1016/j.mtcomm.2020.101546.

[7] Leissa, A. W. (1985). *Buckling of Laminated Composite Plates and Shell Panels.* Ohio: Air Force Wright Aeronautical Laboratories

[8] Timoshenko S. & Gere J. M. (1963). *Theory of Elastic Stability* (2nd ed.). McGraw-Hill.

[9] Hassan Ahmed Hassan, A. and Kurgan, N. (2019). Modeling and Buckling Analysis of Rectangular Plates in ANSYS. International Journal of Engineering and Applied Sciences, 11 (1), 310-329. DOI: 10.24107/ijeas.531011

[10] Pouladkhan, Ali Reza (2011). "Numerical Study of Buckling of Thin Plate". International Conference on Sustainable Design and Construction Engineering. Vol. 78, Issue: 1, Pp. 152 – 157.

[11] Chow, Fong-Yen and Narayanan, Rangachari, "Buckling of Plates Containing Openings" (1984). CCFSS Proceedings of International Specialty Conference on Cold-Formed Steel Structures (1971 - 2018). 1. https://scholarsmine.mst.edu/isccss/7iccfss/7iccfss-session2/1

[12] Uslu, F, Saraçoğlu, M. H. & Albayrak, U. (2022). Buckling of Square and Circular Perforated Square Plates under Uniaxial Loading. Journal of Innovations in Civil Engineering and Technology (JICIVILTECH), 4(2), 61-75.

[13] Tsai, Stephen W. & Hahn, H. Thomas. (1980). *Introduction to Composite Materials*. Westport, Conn: Technomic Pub

[14] Tsai S. W. (1964). *Structural Behavior of Composite Materials*. NASA.

[15] Kaw A. K. (2006). *Mechanics of Composite Materials* (2nd ed.). Taylor & Francis.

[16] Whitney, J. (1987). *Structural Analysis of Laminated Anisotropic Plates* (1st ed.). Routledge. https://doi.org/10.1201/9780203738122

[17] Kassapoglou C. (2013). *Design and Analysis of Composite Structures: With Applications to Aerospace Structures* (2nd ed.). John Wiley & Sons.

[18] Nemeth, M.P. (1986). Importance of Anisotropy on Buckling of Compression-Loaded Symmetric Composite Plates. *AIAA Journal*, *24*, 1831-1835.

[19] Doğan, A. (2020). Buckling Analysis of Laminated Composite Plates Under the Effect of Uniaxial and Biaxial Loads. Turkish Journal of Engineering, 4 (4) , 218-225 . DOI: 10.31127/tuje.665156

[20] Aloulou, Wala & YILDIRIM, Bora & El-Borgi, S. & Zghal, Ali. (2009). Buckling of an orthotropic graded coating with an embedded crack bonded to a homogeneous substrate. International Journal of Solids and Structures - INT J SOLIDS STRUCT. 46. 1890-1900. 10.1016/j.ijsolstr.2009.01.001.

[21] Xiang, Song & Wang, J. & Ai, Y. & Li, G.-Ch. (2015). Buckling Analysis of Laminated Composite Plates by Using Various Higher-Order Shear Deformation Theories. Mechanics of Composite Materials. 51. 10.1007/s11029-015-9534-3.

[22] Nemeth, M.P. (1988). Buckling behavior of compression-loaded symmetrically laminated angle-ply plates with holes. *AIAA Journal*, *26*, 330-336.

[23] Z. Y. Han, Z. L. Cao & H. Y. Fu (2015) Buckling analysis of laminated composite plates with variable fibre orientation angle, Materials Research Innovations, 19:sup5, S5-836-S5-842, DOI: 10.1179/1432891714Z.0000000001204

[24] Georgantzinos, Stelios K., Panagiotis A. Antoniou, Georgios I. Giannopoulos, Antonios Fatsis, and Stylianos I. Markolefas. 2021. "Design of Laminated Composite Plates with Carbon Nanotube Inclusions against Buckling: Waviness and Agglomeration Effects" *Nanomaterials* 11, no. 9: 2261. https://doi.org/10.3390/nano11092261

[25] Reddy, B. , Ramji, K. , Satyanarayana, B. (2011). 'Free Vibration Analysis of Carbon Nanotube Reinforced Laminated Composite Panels'. World Academy of Science, Engineering and Technology, Open Science Index 56, International Journal of Mechanical and Mechatronics Engineering, 5(8), 1616 - 1620.

[26] Taş, Hamza & Soykok, Ibrahim. (2018). Effects of Carbon Nanotube Inclusion into the Carbon Fiber Reinforced Laminated Composites on Flexural Stiffness: A Numerical and Theoretical Study. Composites Part B: Engineering. 159. https://doi.org/10.1016/j.compositesb.2018.09.055

[27] Lei, Z.X. & Zhang, L.W. & Liew, K.. (2016). Buckling analysis of CNT reinforced functionally graded laminated composite plates. Composite Structures. 152. 10.1016/j.compstruct.2016.05.047.

[28] Ouinas, Djamel & Achour, Belkacem. (2013). Buckling analysis of laminated composite plates [(θ/-θ)] containing an elliptical notch. Composites Part B: Engineering. 55. 575-579. 10.1016/j.compositesb.2013.07.011.

[29] Kumar, R. A., Jacob, C. V., Lakshminarayana, N., Puneeth, B. M., & Nagabhushana, M. (2009). Buckling analysis of woven glass epoxy laminated composite plate. *M Tech Thesis NIT Rourkela.*

[30] Jones R. M. (1999). *Mechanics of Composite Materials* (2nd ed.). Taylor & Francis.

[31] Affdl, J.C.H. and Kardos, J.L. (1976), The Halpin-Tsai equations: A review. *Polym Eng Sci*, 16: 344-352. https://doi.org/10.1002/pen.760160512

[32] Georgantzinos SK, Giannopoulos GI, Markolefas SI. Vibration Analysis of Carbon Fiber-Graphene-Reinforced Hybrid Polymer Composites Using Finite Element Techniques. *Materials*. 2020; 13(19):4225. https://doi.org/10.3390/ma13194225

[33] Komur, Mehmet & Sen, Faruk & Ataş, A. & Arslan, Nurettin. (2010). Buckling analysis of laminated composite plates with an elliptical/circular cutout using FEM. Advances in Engineering Software. 41. 161-164. 10.1016/j.advengsoft.2009.09.005.

[34] Rocha, Luiz & Isoldi, Liercio & Real, Mauro & dos Santos, Elizaldo & Correia, Anderson & Lorenzini, Giulio & Biserni, Cesare. (2013). Constructal design applied to the elastic buckling of thin plates with holes. Central European Journal of Engineering. 3. 10.2478/s13531-013-0105-x.

[35] Abolghasemi, S., Eipakchi, H. & Shariati, M. An analytical solution for buckling of plates with circular cutout subjected to non-uniform in-plane loading. Arch Appl Mech 89, 2519–2543 (2019). https://doi.org/10.1007/s00419-019-01592-3

[36] Srivastava, A. & Datta, Prosun. (2006). Elastic stability of square stiffened plates with cutouts under biaxial loading. Int. J. of Applied Mechanics and Engineering. 11. 421-433.